Synthesis of ceramic tiles with alkali-activated materials

By

Haoming Wu

Additional Research Project

in Civil Engineering

at the Delft University of Technology,

Supervisor:	Dr. Guang Ye	TU Delft
	Dr. Hua Dong	TU Delft

TU Delft

Contents

Abstract

In this study, the feasibility of fabricating ceramic tiles with alkali-activated materials (AAMs) was investigated by the as-cast metakaolin based geopolymer (GP) and alkali-activated slag (AAS), in the perspective of crystallization, integrity and flexural strength. After heat treatment at 800 ℃, considerable extent of crystallization of nepheline, low-carnegiete was found in GP; while akermanite, merwinite and nepheline was found in AAS. The crystallization behavior is highly dependent on the mix proportions as well as the curing conditions. Longer curing time and suitable curing temperature is favorable for the crystallization of the AAMs after sintering. Additionally, RHA can be used as an alternative silica source to substitute the commercial silicate solution and its influence on crystallization is minor. A very important observation is that the results indicated the considerable contribution and significance of alkali-activated reaction before the heat treatment to the crystallization. On the other hand, most of the samples showed considerable cracking due to sintering. Only few of the AAS mixtures exhibited relative acceptable integrity but had poor flexural strength due to the internal cracks forming before sintering. The extent of cracking got more serious in the mixtures with denser microstructure. The driving force behind the cracking might be attributed to the capillary action and vapor pressure. The cracks could be healed to an extent by the heat treatment but the healing efficiency seemed to be poor. It was concluded that AAMs do have the potential to fabricate ceramic tiles, but the as-cast method seems to be unfeasible for the ceramic tile fabrication due to the considerable cracking tendency.

1 Introduction

1.1 Brief introduction

Ceramic tile is one of the most widely used building materials. Ceramic tiles' production has sharply increased in recent years, reaching more than 18 billion sqm in 2021 [1]. On the other hand, the production of ceramic tiles has a significant environmental impact due to intensive energy consumption with current fabrication technology.

With the increasing attention on the environmental impact and sustainability, in the Paris agreement, all 197 UNFCCC members have a joint global commitment to deliver net zero carbon emission in the second half of the century. Afterward, the European climate law states the target to achieve carbon neutrality by 2050. Considering the high environmental impact and large market of ceramic tile, its production seems to be a pain spot for this target, and some action needs to be taken.

In order to solve this problem, alkali-activated technology can be a candidate. Alkali-activated material (AAM) is a binder system derived from the chemical reaction of a liquid alkali metal source (referred to as activator) with solid aluminosilicate powers (referred to as precursor). Two widely used AAMs are the geopolymer (GP) derived from metakaolin, and the alkali-activated slag (AAS) derived from slag. AAMs were initially developed to be the alternative to ordinary Portland cement (OPC) and used in construction. During the investigation of the thermal behavior of AAMs, it was found that the phase of AAMs can reform from amorphous to crystalline upon heating at a temperature lower than 1000℃, which is considerably lower than the temperature required in conventional ceramic fabrication. Therefore, research on fabricating ceramic materials with alkali-activated technology started to emerge recently.

In this study, the feasibility of fabricating architectural ceramic tiles with AAMs was preliminary studied.

1.2 Aim and scope of the study

Fabricated ceramic tiles have several critical properties and characteristics, such as crystallization products, integrity, strength, hardness, thermal resistance, corrosion resistance, etc. These properties are influenced by the composition and production process of AAMs. To be more specific, it depends on many factors, including the selection of precursor and activator, the detailed mix design, curing time and temperature, drying time and temperature, production method, sintering time and temperature curve, etc. It is impossible to address all these factors in this preliminary research. Thus, the scope of the research is narrowed down.

The metakaolin and blast furnace slag are selected as the precursor. Although metakaolin is an industrial product, it was more thoroughly investigated in the previous literature due to its purity, simplicity, and consistency in chemical composition. On the other hand, blast furnace slag is an industrial by-product widely used to replace the OPC in construction.

The selection of activator is limited to the sodium silicate and sodium hydroxide solution, which were most widely used in previous AAMs studies. Potassium and cesium-based activator are also used in producing high-tech ceramic and ceramic composite in literature. But considering their high price and high sintering temperatures, it is not wise to be selected as an activator to produce architectural ceramic

tiles. Sodium carbonate solution is also a choice to produce AAMs, but it is not included because of its unfavorable slow early-age reaction [2].

Playing a decisive role in the resultant product microstructure, the fabrication method significantly influences the ceramic tiles' resultant properties, such as mechanical properties and integrity. The as-cast method and powder metallurgy method are two commonly used fabrication methods in the limited literature. In this preliminary research, the as-cast method will be selected, considering the simplicity, less process steps, availability of equipment, and fewer variables in the process.

The objective of this research is to preliminarily investigate the feasibility of using alkali-activated materials technology to fabricate ceramic tiles. The main focus will be on the crystallization, integrity, and strength of the products with different mix designs of AAMs and production processes.

2 Literature review

2.1 Background

Ceramics is one of the indispensable products in people's lives and has been invented for thousands of years. It is widely used in many fields, such as architecture, biomedical science, aerospace, etc. Ceramic tile is one of the most traiditional application of ceramic fabrication and one of the most widely used decoration products [1, 3]. Traditional ceramic tiles are fabricated with clay and other natural minerals by a series of heat treatments. Depending on the intended functionality, the highest firing temperature ranges from 1100 to 1500°C. Typical features of ceramic tiles are hard, brittle, chemical-resistant, heat-resistant, etc. [4]. Ceramic tile has a huge and rapidly growing market [1]. However, with the increasing awareness of the environment and sustainability, the environmental impact of the fabrication of ceramic tiles could be a pain point. According to the life cycle assessment, the environmental impact of ceramic tiles fabrication is significant, especially in the impact category of global warming. This is caused by the intensive use of energy and CO_2 emission during the fabrication as well as transportation of raw materials [3, 5, 6]. Therefore, with the increasing concern on the environment, some efforts might be taken to reduce the environmental impact of the huge and rapid-growing ceramic tiles market.

Alkali-activated material (AAM) is a binder system derived by the reaction of a liquid alkali metal source (referred to as activator) with solid aluminosilicate powers (referred to as precursor) under the range of normal temperature lower than 100°C [7, 8]. AAMs are initially developed as the alternative of ordinary Portland cement (OPC) to reduce the environmental impact of the construction. Because of the nature of the alkali-activated reaction, any materials containing mostly reactive silica and alumina can be potential raw materials to produce AAMs, such as metakaolin, blast furnace slag, fly ash, and rice-husk ash. For this reason, the alkali-activated technology offers the possibility of re-using aluminum silicate industrial waste and by-products. In recent decades, alkali-activated technology attracted great interest from researchers.

During the investigation of the thermal behavior of AAMs, it was discovered that the phase of AAMs could transform from amorphous to crystal. Depending on the selected precursors and activators, different minerals can be formed in AAMs after reaching elevated temperature, such as nepheline from sodium-activated geopolymer (Na-GP) [9], leucite from potassium-activated geopolymer (K-GP) [10, 11], pollucite from cesium activated geopolymer (Cs-GP) [12, 13], akermanite from alkali-activated slag (AAS), etc. The crystallization temperature of AAMs depends on the composition but is generally lower than 1000°C, which is lower than many conventional ceramic tiles firing temperatures [14-16]. This characteristic allows fabricating ceramic tiles with lower energy consumption.

Depending on the purposes of the application, there are different requirements for ceramic tiles [17, 18]. Generally, the requirements of ceramic tiles focus on three aspects: (a) the dimensions and surface quality, e.g., the accuracy of the dimensions and the integrity of the products; (b) the physical properties, e.g., water absorption, mechanical properties, thermal properties, etc.; and the (c) the chemical properties, e.g., the resistance to chemicals as well as the release of harmful substances.

Mechanical property is one of the crucial properties of ceramic tiles. In accordance with EN 14411 [17], depending on the classification of the ceramic tiles, the flexural strength requirement ranges from 8MPa to 35MPa. From the perspective of AAMs, the lower limit of flexural strength is achievable after curing under normal temperature for a certain period. Therefore, AAMs have already shown the potential of fabricating non-baking ceramic tiles. On the other hand, previous research also shows

good mechanical properties of heat-treated AAMs. He et al. [12] produced leucite samples from K-GP with 70MPa flexural strength, and Xie et al. [19] also produced leucite samples with 140MPa. Therefore, from the perspective of mechanical properties, AAMs have the potential to fabricate ceramic tiles.

Hard and brittle are also typical features of ceramic tiles. Depending on the purpose of the application, the Moh's hardness of ceramic tiles is mostly in the range of 5-6, which is similar to the hardness of mineral apatite or feldspar. When alkali-activated technology is used to fabricate ceramic tiles, the products are likely to fulfill these features. The nepheline derived from Na-GP, and the leucite from the K-GP are in the feldspar group and have a Moh's hardness of around 6, while the akermanite derived from AAS has a hardness slightly higher than 6.

Therefore, there is sufficient motivation to investigate the potential of using alkali-activated technology as a new ceramic tiles fabrication technology and have some feasibility study.

2.2 Evolution of physical properties during heating

The physical evolution of AAMs during heating is usually focused on the aspects of the variation of mass and volume stability. And this has been investigated in several literature.

2.2.1 General information

The shrinkage of GP paste during heating has been investigated with dilatometry in literature [20]. Significant shrinkage is observed when heating GP to an elevated temperature due to capillary action, dehydroxylation, vicious sintering, etc. The behavior highly depends on the component of the GP, such as the nominal Si/Al ratio [21, 22] and the type of cations [12, 21]. In general, the length of evolution can be categorized into different regions and will be discussed later. A typical thermal shrinkage curve of GP is shown in Figure 2.1 [10].

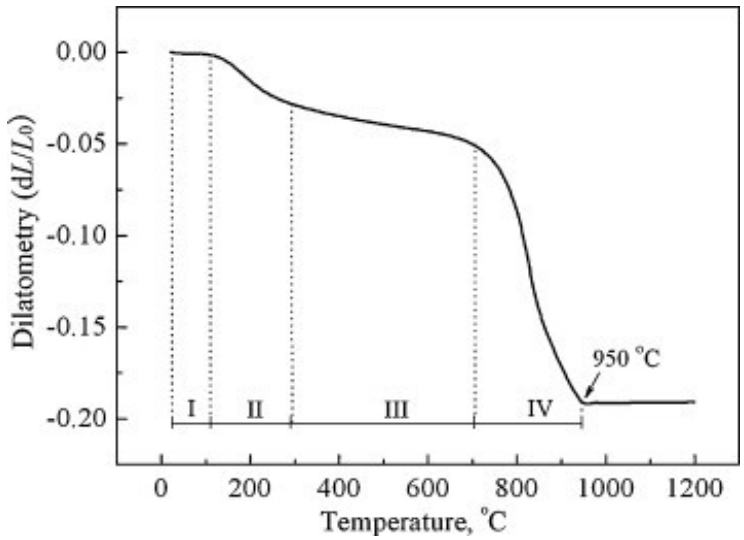

Figure 2.1 Dilatometry of K-GP Sample heated at 5 °C/min up to 1200 °C, adapted from [10]

On the other hand, the information concerning the volume change of AAS paste with increasing temperature is scarce. In contrast to GP which shows clearly different behavior in different temperature range, the length evolution of AAS paste measured by dilatometry have a linear characteristic [23, 24], as shown in Graph 2.2.

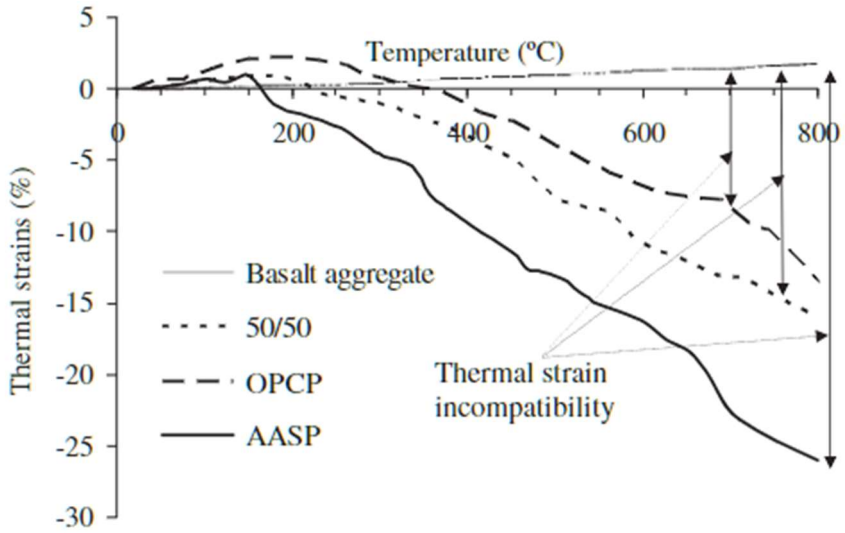

Figure 2.2 Dilatometry test of several samples up to 800 °C, where AASP in solid line stands for the AAS paste, adapted from [23]

The mass evolution of GP [10, 11, 13, 21, 22, 25, 26] and AAS [26-28] during heating has been investigated with thermogravimetry in literature. A comparative study of thermal behavior of alkali-activated slag/metakaolin paste has been done by Burciaga-Díaz, O. and Escalante-Garcia, J.I [26]. The thermogravimetric analysis result is shown in Figure 2.3. In the figure, the first number of the specimen's name stands for the content of slag in the paste, and the second number stands for the content of metakaolin in the paste, by the weight percentage of precursor.

The mass loss during the heating is basically the result of the evaporation of free water, bond water, and the dehydroxylation water of the condensation of T-OH groups (T = Si, Al). In contrast to thermal shrinkage, the characteristic of mass evolution is similar regardless of the composition [21]. According to the literature, the bulk of the water loss occurred at temperatures ranging from RT to around 250°C. Considering the onset temperature of dehydroxylation is generally above this value, it is concluded that most of the evaporated water in the system is free water and bond water.

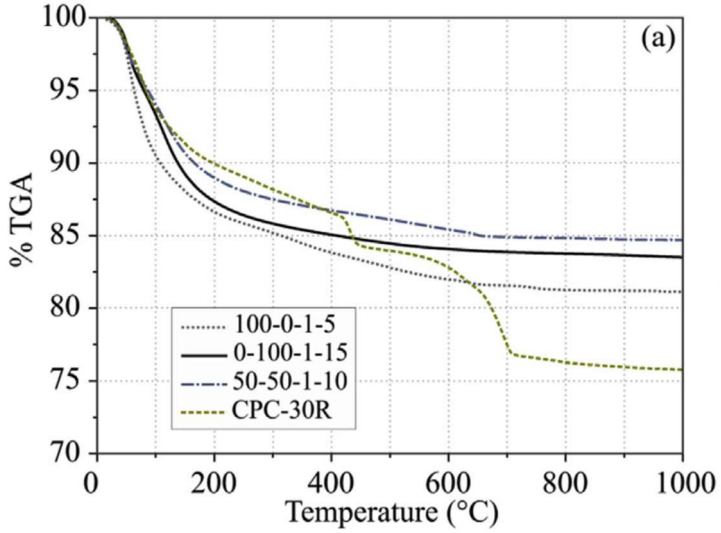

Figure 2.2 Thermogravimetric analysis of the AAMs binders 100-0 (100% slag), 50-50 (50% slag with 50% metakaolin), 0-100 (100% metakaolin) and a OPC reference CPC-30R heated at various temperatures. [23]

2.2.2 Dividual regions of physical evolution during the heating

Although the thermal behavior of GP is closely related to the component, it can be generally categorized into four regions [10, 11, 13, 21, 22], as indicated in Figure 2.3 [13].

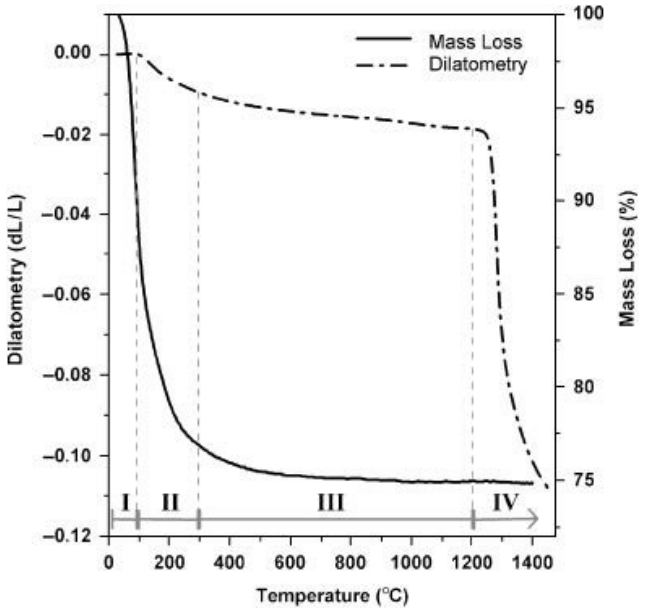

Figure 2.3 Dilatometry and TG results for Cs-GP heated at 10℃/min up to 1450℃, adapted from [13].

The temperature ranging from room temperature to around 100°C is categorized into Region I. Depending on the initial water content, considerable mass loss can be observed in the region. On the other hand, the volume is very stable. It is believed that most of the mass loss in the region is the evaporation of free water in large pores and the surface. Because the evaporation occurs at the large pores, no capillary stress will be created in this stage, leading to high volume stability [13, 29].

Region II begins with the onset of shrinkage at around 100°C and ends at around 300℃.. Significant mass loss can be observed in this temperature range. The mass loss is mainly attributed to the release of water from capillaries and chemically bound water. Consequently, capillary action occurs, causing moderate shrinkage observed in the test [30].

Region III starts at approximately 300℃ and lasts until the initiation of a significant shrinkage, which is the indication for the onset temperature of region IV. In region III, concomitantly nominal mass loss and shrinkage can be observed. This mass loss is attributed to the elimination of water created by the condensation of T-OH groups (T = Si, Al), also known as dehydroxylation. With the reaction between hydroxyl groups, the creation of T-O-T linkage results in the joining of the surface groups and densifying the gel skeleton, and further results in the nominal shrinkage observed in this stage.

Region IV involved the temperature above the onset temperature where a significant shrinkage occurs, as shown in Figure 2.3. This onset temperature is highly dependent on the composition of AAMs, for instance, the Al/Si ratio [21, 22] and the type of cations [21, 25] . The significant shrinkage in this stage is attributed to viscous sintering. During the viscous sintering, the densification can be observed by a significant reduction in the BET surface area and pore volume [10, 13, 22], and the closure of pores and cracks that are observed by SEM [10, 13, 25].

2.2.3 Influencing factors on the physical evolution during heating

The thermal behavior of AAMs highly depends on factors like mix proportion and heating process. In another perspective, the desirable thermal response and product properties could be tailored by modifying the mix design.

P. Duxson et al. investigated a series of geopolymer samples with varying nominal Si/Al ratios in the range of 1.15 - 2.15. Before heating, the microstructure of synthesized geopolymer is highly dependent on the Si/Al ratio [31]. The GP with a Si/Al atomic ratio of 1.15 and 1.40 has a porous microstructure

comprising dense particulates and large interconnected pores. GP with Si/Al atomic ratio of 1.65, 1.90, 2.15 has a much more homogenous microstructure and much smaller individual pores. The cause behind this was attributed to the difference in the mechanism of gepolymerization under the condition of higher soluble silicon in the activating solution [31]. As a result, Young's modulus and compressive strength of the GP samples also increase with increasing Si/Al ratio. When subjected to heating, with an increasing Si/Al atomic ratio, the final extent of shrinkage and the density of the GP increases [21, 22]. The onset temperature of sintering also becomes lower when the Si/Al ratio is high, indicating that the GP becomes less refractory.

The effect of heating rate is revealed by P. Duxon et al. [21, 22] and P.He et al. [12]. For the thermal shrinkage, the heating rate seems to not influence region I -III. For the densification in region IV, the extent of densification increases with the increasing heating rate. On the other hand, the heating rate significantly influences the integrity of the products, especially the heating rate in the region I - III. With a lower heating rate, the cracking potential of K-GP decreased. The reason was attributed to a more even temperature and water evaporation distribution among the GP matrix. The initiation, propagation, and recovery of cracks are also discussed [12]. However, not much solid evidence was provided in the paper.

The influence of the alkali cation on thermal shrinkage is studied in the literature. P. Duxon et al. [21] compared the behavior of Na-GP (100% Na), NaK-GP (50% Na, 50% K), and K-GP (100%K) under a constant heating rate. The thermal shrinkage of K-GP is smaller than Na-GP, regardless of the Si/Al atomic ratio. In the case of partial substitution, compared to Na-GP, the NaK-GP specimen with low Si/Al atomic ratio (≤1.65) has a lower extent of thermal shrinkage, but for higher Si/Al ratio samples, the extent of shrinkage is similar. JL. Bell et al. [11, 13] studied the thermal behavior of K-GP and Cs-GP with the same chemical formula ($R_2O \cdot Al_2O_3 \cdot 4SiO_2 \cdot 11H2O$, where R = K or Cs). The result shows that the thermal shrinkage of Cs-GP is smaller than K-GP. He et al. [25] studied the effect of Cs substitution (0% - 40%) on the thermal evolution of K-GP with the composition of $R_2O \cdot Al_2O_3 \cdot 5SiO_2 \cdot 11H2O$. It was found that the substitution of Cs considerably reduces the extent of shrinkage at vicious sintering. The onset temperature of densification is also dependent on the cation type. According to the literature, the onset temperature of densification is in the order of Cs-GP > K-GP > Na-GP. For a binary system, P. Duxon et al. [21] found the onset temperature of densification is in the order of K-GP > NaK-GP ~ Na-GP, for all the samples ($1.15 \leq Si/Al \leq 2.15$). On the other hand, He et al. [25] observed an increasing onset temperature of region IV of K-GP with increasing Cs substitution. In general, using/incorporating alkali cations with higher atomic numbers will make the GP become more refractory by having a lower extent of thermal shrinkage and a higher onset temperature of densification. This phenomenon is attributed to the higher softening temperature of gel caused by the increased strength of Al-O bonds due to the presence of cations with higher atomic numbers [21, 32]. For the KCs-GP system, an additional driving force might be the crystallization before the onset of sintering. The addition of Cs induces many small nuclei in the matrix, which later served as the crystallization site for the crystallization and lowered the crystallization temperature. With the crystallization before the onset of sintering, the viscosity of the matrix is increased and the GP becomes more refractory [25].

2.3 Crystallization after heating

The crystallization behavior of AAMs subjected to elevated temperature has been investigated by XRD analysis in literature and the results will be shown in this section.

2.3.1 Alkali-activated metakaolin (geopolymer)

The phase evolution of geopolymer derived by alkali-activated metakaolin has been systematically studied. Depending on the composition of the GP, minerals of nepheline, kaliophilite, leucite, pollucite, etc., can be generated after heat treatment.

P. Duxson et al. [33] investigated a series of geopolymers samples prepared by sodium silicate-activated metakaolin with a nominal composition of $NaAlO_2(SiO_2)_z \cdot 5.5H_2O$ ($1.15 \leq z \leq 2.15$) treated at different temperatures up to 1000℃. Faujasite ($Na_7[Al_7Si_{17}O_{28}] \cdot 32H_2O$) was found in Na1.15 samples (z=1.15) when the temperature was below 500℃. After heating to a temperature higher than 500℃, all the faujasite was destroyed. With further increasing the temperature, crystallization of nepheline ($NaAlSiO_4$) was found in all the samples. The crystallization temperature of nepheline increases with increasing Al/Si atomic ratio, ranging from 600℃ to 800℃. This trend contrasts with the onset temperature of viscous sintering, indicating that the relationship between crystallization and structural densification is relatively weak.

P. Duxson et al. [34] also investigated the phase evolution of a series of potassium-based geopolymers when heated up to 1000℃. The nominal composition of the samples is $KAlO_2(SiO_2)_z \cdot 5.5H_2O$ ($1.15 \leq z \leq 2.15$). For the lowest Si/Al atomic ratio samples K1.15, only kaliophilite ($KAlSiO_4$) was found as the crystalline phase. On the other hand, only leucite ($KAlSi_2O_6$) was found in the K2.15 samples. For the other samples, both kaliophilite and leucite can be found during the heat treatment. It is also observed that the degree of crystallization decreases with increasing Si/Al atomic ratio, which is identical to the observation in sodium-based geopolymer. However, there is little fundamental explanation on this phenomenon. The author inferred that this might be due to the difference in microstructure that controls the ability of gel to rearrange and crystallize.

JL. Bell et al. [11] investigated the formation of leucite from geopolymer with the nominal composition of $K_2O \cdot Al_2O_3 \cdot 4SiO_2 \cdot 11H_2O$, which has the identical stoichiometry composition of leucite. After heat treatment, in addition to the leucite, a minor amount of kalsilite (KAlSiO4) was also found in the the XRD pattern. It was also found that the weight fraction of formed leucite increased with increasing soaking temperature or soaking time.

The crystallization behavior of geopolymer derived from cesium silicate-activated metakaolin was investigated by JL. Bell et al. [13]. Geopolymer with the composition $Cs_2O \cdot Al_2O_3 \cdot 4SiO_2 \cdot 11H_2O$ crystallized into pollucite ($CsAlSi_2O_6$) upon heating. The density of GP reached approximately 98% of the theoretical density of pollucite when heated to 1600℃.

It is noticed that most of the mix proportion in literature has an R_2O/Al_2O_3 ratio equalling to 1. This choice is made considering chemical reaction and the crystallization products. H. Rahier et al. [35] studied the effect of R_2O/Al_2O_3 ratio (R= Na / K) on the reaction of metakaolin with DSC and NMR. The reaction heat of the geopolymerisation increases with increasing R_2O/Al_2O_3 ratio until the nominal cation ratio of GP reaches unity. And no greater heat is released with further increment. It was concluded that one cation is from the activator is needed for each Al from metakaolin from the stoichiometry point of view. From the perspective of crystallization, it is found that all the crystallization products from geopolymer have an R_2O/Al_2O_3 ratio equal to one. And it can be inferred that the deviation of R_2O/Al_2O_3 ratio from one will only result in a more amorphous phases in the products [22].

2.3.2 Alkali-activated slag

The crystallization behavior of AAS is not systematically studied because most of the research interests before are on its application in construction. The chemical composition of blast furnace slag is not as

pure as metakaolin; therefore, the phase composition of thermal-treated AAS is also much more complicated. The main reaction product of AAS is C-(A)-S-H gel. However, to the author's best knowledge, there is scarce literature investigating the thermal behavior of different C-(A)-S-H gel under elevated temperatures.

F. Puertas et al. [36] investigated the thermal behavior of an AAS paste with alkali content (Na_2O to slag ratio, N/B) equal to 4% and modulus (SiO_2 to Na_2O ratio, Ms) equal to 1.18. The AAS paste was cured at 20℃ with 99% RH for 28 days before the heat exposure. After exposed to 1200℃, the sample had crystalline phase consists of akermanite ($Ca_2Mg[Si_2O_7]$), gehlenite ($Ca_2Al[AlSiO_7]$), and nepheline.

P. Rovnanik et al. [37] investigated the behavior of an AAS paste subjected to an elevated temperature ranging from 200 to 1200℃. The AAS paste, with Ms = 1.95 and N/B = 5.4%, was subjected to underwater curing for 27 days after de-molding at 20℃. The blast furnace slag and unheated AAS paste are generally amorphous, with minor amounts of merwinite ($Ca_3MgSi_2O_8$) and quartz (SiO_2). When exposed to elevated temperatures up to 600℃, only partial dehydration and decomposition of C-A-S-H were found. With the temperature further increased, the dehydration and decomposition of C-A-S-H fully completed, and the crystalline phase started to emerge. Akermanite was found to be the dominant crystalline phase in the samples. A minor extent of crystalline wollastonite ($Ca_3Si_3O_9$) and diopside ($CaMgSi_2O_6$) was also observed. It was found that the crystalline phase is only formed from the calcium magnesium silicates, while practically all the aluminum is incorporated in the glass phase. And the glass phase after heat treatment only accounted for 12.5% of the whole matter.

SA. Bernal et al. [38] investigated the thermal behavior of AAS paste samples with Ms = 2.4 and N/B = 5%. The low Mg, blast furnace slag, was activated by sodium silicate solution prepared with 1) commercial water glass solution, 2) silica fume and NaOH solution, 3) rice husk ash (RHA) and NaOH. The pastes were cured at 27±2℃ for 28 days and exposed to 800℃ and 1000℃ afterward. Gehlenite was found to be the dominant crystalline phase in the heated samples. Minor levyne and wollastonite were also found. The intensity of the reflection peaks of AAS exposed to 1000℃ was significantly stronger than those from AAS exposed to 800℃. The XRD patterns of AAS prepared by commercial water glass and AAS prepared by silica fume did not show a significant difference. In contrast, the AAS prepared by RHA showed a higher content of wollastonite crystal.

AM. Rashad et al. [27] investigated the thermal resistance of 28-day AAS pastes samples with Ms = 1.7 and different N/B ratios from 2.5% to 10.5%. The XRD patterns of sample N3.5% and sample N6.5% were compared. The patterns were similar, and crystallization of akermanite, gehlenite and merwinite were found. It seems that the N/B ratio did not create a significant influence on the crystallization. This might be attributed to the constitution of reaction products of AAS. At high pH environments, the presence of Ca will degrade N-A-S-H and form C-A-S-H [39]. Sodium is not cooperated in the main reaction products, and therefore has little influence on the crystallization behavior.

2.4 Fabrication and resultant properties of AAMs ceramic

Although the alkali-activated technology offers a novel path to the sythesis of ceramic products, to the author's knowledge, not many attempts have been made on the industrial application. In addition, there is also not much information concerning the physical and chemical properties of the AAMs ceramic within the scope of this study, which is the sodium silicate activated materials.

The method of fabrication has a significant impact on the properties of the products [12, 40]. The typical fabrication methods for AAMs ceramic are the as-cast method and powder metallurgy method. In the as-cast method, the fresh AAM paste is cast into the mold, cured, and directly brought to heat

treatment. By this method, the production process is simple, not much equipment is needed, and the possibility of forming the products with complicated final shapes is ensured. However, the cracking potential caused by drying and dehydration is very challenging. There has been only very limited report on fabricating ceramic with proper integrity, and very careful control of the heating rate is required [12]. In the powder metallurgy method, the cured AAMs are first brokes into powders, pressed, and then heated. This method considerably reduces the cracking potential [19, 40]. However, it will lose the advantage of forming complicated shape products, involves more production processes, and creates more costs.

P. Rovnanik et al. [37] investigated the flexural strength of 28 days as-cast AAS paste subjected to an elevated temperature ranging from room temperature to 1200℃, with an interval of 200℃. The flexural strength of AAS at room temperature was around 5 MPa. When subjected to heat treatment, the flexural strength decreased with increasing temperature until 800 ℃. At this point, the lowest flexural strength reached the minimum value of around 2 MPa. On the other hand, when the AAS was further heated to 1000 ℃ and 1200 ℃, the flexural strength considerably increased to around 6 MPa and 9 MPa.

I. Beleña and W. Zhu [41] conducted a nanoindentation study on the Na-Geopolymer before and after exposure to 1000℃. It was found that the mechanical properties of the geopolymer significantly increased thrice after the treatment.

C. Kuenzel et al. [42] investigated the mechanical properties and microstructure of GP mortar prepared with sodium silicate-activated metakaolin and silica sand. The composition of the GP paste is $Na_2O{\cdot}Al_2O_3{\cdot}\ 4SiO_2{\cdot}9H_2O$. The amount of additional sand is of the same mass as the paste. The mortar was cast into an $8\times8\times40mm^3$ plastic mold and cured for 77 days at 22 ± 3℃. The as-cast specimens were dried for 24 hours at 35℃, then they were heated at various temperatures up to 1100 ℃, with a heating rate of 20 ℃/min. Nepheline and carnegiete were found in the specimen after heating to 900 ℃, but reformed/melted into amorphous phases after heating to 1100℃. For the compressive strength, before reaching 800℃, the compressive strength of specimens remained relatively unchanged; when heated at 800-1000℃, the compressive strength of specimens increased; but further heating at 1100℃ decreased the compressive strength again. Similarly, the Vickers hardness of GP mortar increased with increasing temperature until 1000℃, but decreased with further heating. On the other hand, the evolution of flexural strength showed quite a different trend. The heat treatment before 800℃ resulted in a continuous flexural strength decrease, which might be due to the microcracking at the matrix and ITZ. Afterward, the flexural strength stabilized at 750-900℃ and increased when further heated at 1000℃. The mechanism behind this was attributed to the sintering. However, the flexural strength after heat treatment is lower than at room temperature.

R. Ahmad et al. [43] investigated the effect of sintering temperature on the properties of nepheline ceramic produced by GP powders. The powder metallurgy method was used in the study. The GP was cured at 80℃ for 24 hours after casting, crushed into powders by a mechanical crusher, blended with high molecular weight polyethylene (UHMWPE) by a planetary mill, compacted into mold under 5 tons load for 2 min, and finally sintered at various temperatures (900℃, 1000℃, 1100℃ and 1200℃) for 3 hours with a heating rate at 5℃/min. The dosage of UHMWPE is 4% by weight of the GP powders. The nepheline ceramic plates were successfully fabricated. The resultant flexural strength increased with increasing sintering temperature, ranging from 42.5 MPa to 92.0 MPa.

2.5 Objective

Based on the literature, a series of researchers have investigated the fundamental information about ceramic production with alkali-activated technology, such as crystallization and physical evolution during heat treatment. For the topic, the geopolymer derived from metakaolin has been more systematically studied than alkali-activated slag whose focus is construction application. On the other hand, the information on resultant properties and tentative industrial application of AAMs ceramic is still very limited. Nevertheless, some researchers successfully derived AAMs ceramic with proper integrity and desirable mechanical. And the heat treatment temperature was lower than the temperature of conventional ceramic production. These outcomes show that alkali-activated technology creates a potential to produce ceramic in a more environmentally friendly way.

The target of this study is to preliminarily investigate the feasibility of fabricating ceramic tiles with alkali-activated technology. This has never been discussed before, and related information is very limited. Therefore, some fundamental questions needed to be answered in this study to evaluate the feasibility:

- What are the crystals formed after heat treatment?
- How is the integrity of AAMs ceramic after heat treatment, and how to improve?
- What is the mechanical properities of the AAMs ceramic after heat treatment?
- What is the influence of mix proportions and production processes on these characteristics and properties?

These research questions formulated the research framework of this study.

3 Materials and methods

3.1 Raw materials

3.1.1 Metakaolin

Metakaolin is the aluminosilicate source, i.e., precursor, to produce GP. The metakaolin used in the study is purchased from BASF, under the brand name *metamax*. It is a high-reactivity pozzolan material produced by a series of heat treatments at 600 - 900℃ from kaolin. The chemical composition of the metakaolin is determined by the X-ray fluorescence (XRF). The SiO_2/Al_2O_3 ratio of the metakaolin is 1.84, slightly lower than that used in the literature [11, 21]. The details are shown in Table 3.1, and it can be seen that metakaolin is a high-purity aluminosilicate source with minor Ti impurity.

Table 3.1 Chemical composition of metakaolin

Oxide (wt%)						
SiO_2	Al_2O_3	TiO_2	Fe_2O_3	Na_2O	K_2O	Other
50.7	46.8	1.7	0.3	0.3	0.1	0.1

The phase composition of the metakaolin is investigated by X-ray diffraction (XRD), as shown in Figure 3.1. It can be observed that the metakaolin is mostly amorphous, with minor crystalline anatase (TiO_2) as impurity. The particle size distribution of metakaolin is investigated by laser diffraction analyzer, as shown in Figure 3.2. The result shows that metakaolin consists of very fine particles with a relatively narrow size distribution. The d_{10}, d_{50}, and d_{90} of the metakaolin are 1.46 um, 4.37 um and 12.68 um, respectively.

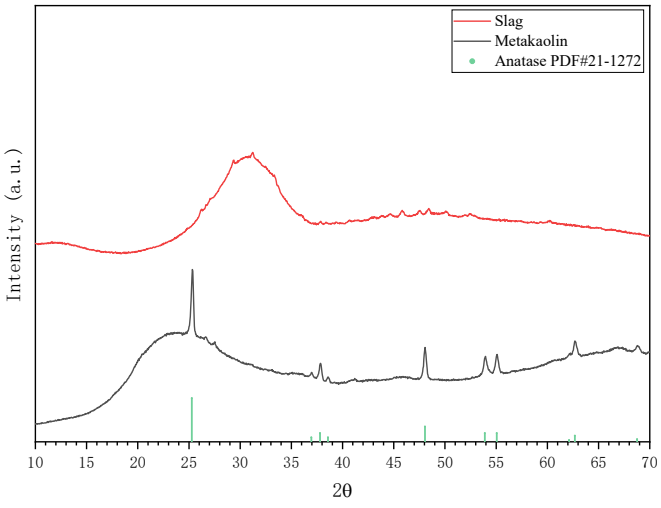

Figure 3.1 X-ray diffractograms for metakaolin and blast-furnace slag

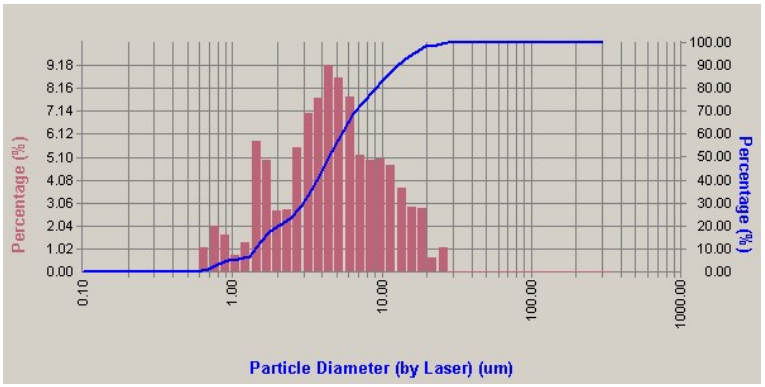

Figure 3.2 Particle size distribution of metakaolin

3.1.2 Blast-furnace slag

Blast-furnace slag (slag) is the precursor to produce alkali-activated slag (AAS). The slag used in the study is provided by Ecocem Benelux BV, an industrial by-product from the manufacturing of iron. The phase composition of the slag is investigated by the XRD, and also shown in Figure 3.1 above. The slag used in this study is amorphous. The chemical composition of the slag is determined by the X-ray fluorescence (XRF) and shown in Table 3.2. As an industrial by-product, slag has a much more complicated chemical composition than metakaolin. The particle size distribution of slag is determined by laser diffraction analyzer, as shown in Figure 3.3. The d_{10}, d_{50}, and d_{90} of the slag are 5.54 um, 20.40 um and 42.54 um, respectively.

Table 3.2 Chemical composition of blast-furnace slag

Oxide (wt%)								
SiO_2	Al_2O_3	CaO	MgO	Fe_2O_3	SO_3	K_2O	TiO_2	Other
31.8	13.3	40.5	9.3	0.5	1.5	0.3	1.0	1.9

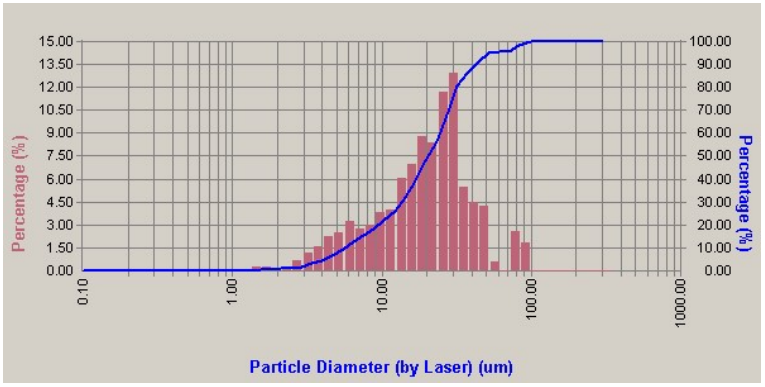

Figure 3.3 Particle size distribution of blast-furnace slag

3.1.3 Rice husk ash

Rice husk is the protective covering of rice grains that is separated from the grains during the processing. Rice husk ash (RHA) is produced by the incineration of rice husk. It is a highly reactive pozzolanic material and has been used as supplementary cementitious material and internal curing agent in concrete for many years [44-48]. It is rich in silica and offers the possibility to prepare the sodium silicate activator in an environmental way [38, 47].

The chemical composition by XRF and the phase identification by XRD are available in previous publications and shown in Table 3.3 [45] and Figure 3.4 [48]. RHA is mostly amorphous with a small amount of crystallized quartz.

Table 3.3 Chemical composition of rice hask ash [45]

Oxide (wt%)						
SiO_2	Al_2O_3	CaO	Fe_2O_3	SO_3	K_2O	Other
88.9	0.3	1.7	0.2	0.6	4.2	2.5

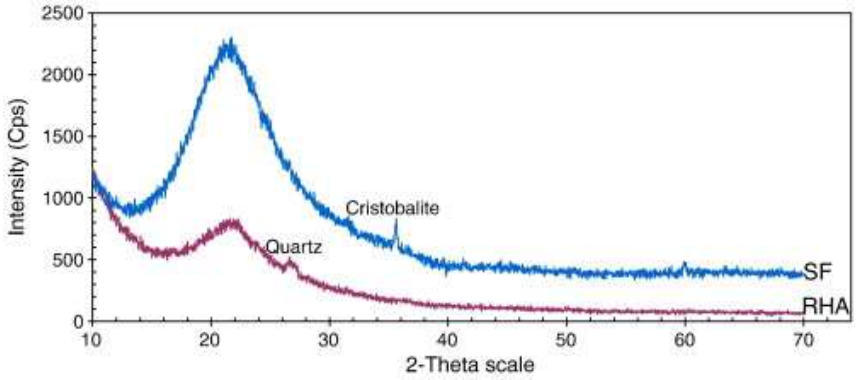

Figure 3.4 X-ray diffractograms for rice husk ash (in red) and silica fume (in blue) [48]

The particle size distribution of RHA is determined by laser diffraction analyzer, as shown in Figure 3.5. The d_{10}, d_{50} and d_{90} of the slag are 21.27 um, 75.47 um, and 116.85 um, respectively.

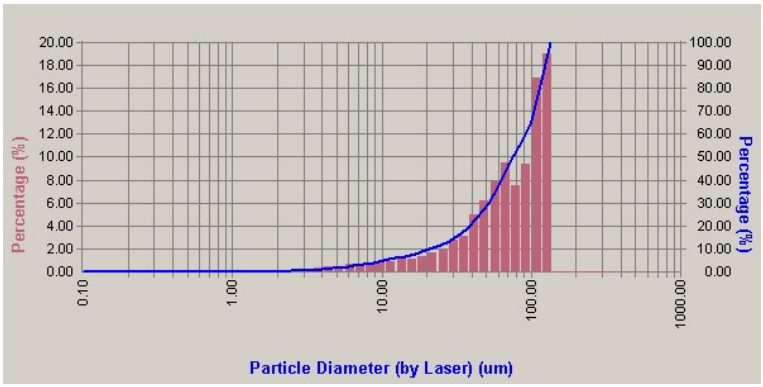

Figure 3.5 Particle size distribution of rice husk ash

3.1.4 Sodium silicate activator solution

The alkali activator solution was prepared with the commercial sodium silicate solution or rice husk ash (RHA), commercial sodium hydroxide solution, and deionized water according to the designed mix proportions shown in the next section. The activator was prepared one day before the mixing to ensure the solution was at ambient temperature when mixing.

3.2 Mix proportion and production process

3.2.1 Geopolymer (GP) mixtures

The mix proportion of GP is generally designed with the Na_2O/Al_2O_3 ratio, SiO_2/Al_2O_3 ratio, and H_2O/Na_2O ratio. The mix design can be written in the form of the combination of oxides, e.g., $Na_2O{\cdot}Al_2O_3{\cdot}4SiO_2{\cdot}11H_2O$ or in stoichiometry, e.g., $NaAlO_2(SiO_2)_4{\cdot}5.5H_2O$. GP with different mix proportions, the effect of curing conditions, and the effect of RHA substitution are investigated.

The Na_2O/Al_2O_3 ratio is controlled to be one, as in most literature [10-13, 21, 25, 34]. The H_2O/Na_2O ratio is taken as 13 after a series of trail mixing, considering the workability of all the mixtures. Samples with H_2O/Na_2O ratio equals to 11 and 9 are also included to investigate the influence on integrity.

Factor analysis is conducted on the Si/Al ratio (i.e., SiO_2/Al_2O_3 ratio) of the GP $Na_2O{\cdot}Al_2O_3{\cdot}zSiO_2{\cdot}13H_2O$. The variety of the Si/Al ratio is achieved by the variation of activating solution composition. The range of Si/Al is set to be 0.86 to 2.0, with a selected interval. The details information is shown is Table 3.3.

Table 3.3 GP mixtures with variation of Si/Al ratio and H2O/Na2O ratio

	Mixtures						
	NaMK-NH	**NaMK-1.0**	**NaMK-1.25**	**NaMK-1.5**	**NaMK-1.75**	**NaMK-1.25-11w**	**NaMK-1.25-9w**
N/B	2.8%	2.8%	2.8%	2.8%	2.8%	2.8%	2.8%
Ms	**0.00**	**0.16**	**0.66**	**1.16**	**1.66**	0.66	0.66
Na/Al	1	1	1	1	1	1	1
Si/Al	**0.92**	**1.00**	**1.25**	**1.50**	**1.75**	1.25	1.25
H_2O/Na_2O	13	13	13	13	13	**11**	**9**
Curing temp.	70°C	70°C	70°C	70°C	70°C	70°C	70°C
Curing time	3 days	3 days	3 days	3 days	3 days	3 days	3 days

The curing temperature has a considerable effect on the properties of derived GP. Because metakaolin has a lower reactivity than OPC and slag, heat curing is usually used to pursue a higher reaction speed [49]. The curing temperature in the literature is highly varied from room temperature to even higher than 100°C. S. For this study, a factor analysis will also be conducted on the curing temperature. Curing temperatures 20°C, 45°C, 70°C, and 95°C are used on the selected mixture NaMK-1.25, as shown in Table 3.4. The temperature control has an accuracy of ±5°C.

Table 3.4 GP mixtures with the variation of curing temperature and curing time

	Mixtures						
	NaMK-1.25 -20°C	**NaMK-1.25 -45°C**	**NaMK-1.25 -70°C**	**NaMK-1.25 -95°C**	**NaMK-1.25 -1d**	**NaMK-1.25 -3d**	**NaMK-1.25 -7d**
N/B	2.8%	2.8%	2.8%	2.8%	2.8%	2.8%	2.8%
Ms	0.66	0.66	0.66	0.66	0.66	0.66	0.66
Na/Al	1	1	1	1	1	1	1
Si/Al	1.25	1.25	1.25	1.25	1.25	1.25	1.25
H_2O/Na_2O	13	13	13	13	13	13	13
Curing temp.	**20°C**	**45°C**	**70°C**	**95°C**	70°C	70°C	70°C
Curing time	3 days	3 days	3 days	3 days	**1 day**	**3 days**	**7 days**

The effect of the degree of reaction on the crystallization, achieved by different curing times, is investigated on the selected mixture NaMK-1.25. Meanwhile, the influence on integrity is also investigated. Considering the practice of the industrial application, long curing time is undesirable. In addition, most of the GP reaction finish in the first few days [50]. Therefore, the samples with curing times 1 day, 3 days, and 7 days are investigated, as shown in Table 3.4.

The mixtures mentioned above are produced with the activator prepared with a commercial sodium silicate solution. On the other hand, an environmental way to provide silicate in the activator is using RHA [38]. Therefore, substituting sodium silicate solution with RHA will also be investigated. The addition of RHA in this study follows two different ways. Sample NaMK-1.25-lRHA refers to the situation in which RHA is pre-dissolved in the activator with NaOH solution; sample NaMK-1.25-sRHA refers to the situation in which RHA is added in the precursor during mixing and activated by NaOH solution. In both cases, the amount of RHA powders is determined based on the same stoichiometry amount of silica.

3.2.2 Alkali-activated slag (AAS) mixtures

The mix proportion of AAS paste is generally controlled by the Na_2O/binder ratio (N/B), molar ratio of SiO_2/Na_2O in the activator (Ms), and water/binder ratio (W/B). A factor analysis will be conducted on these mix design parameters for the AAS mixtures.

In general, mixtures with different alkali contents (N/B) and modulus (Ms) are investigated. The mixtures are named NaS-*Ms*-*N/B*. For investigating the crystallization, NaS-(0, 1, 2)-4% and NaS-1-(2%, 4%, 6%) are studied. For the samples characterized in terms of flexural strength, based on the results of integrity, the range is narrowed down, and the interval is halved.

As slag has a higher reactivity, the AAS samples are cured under the temperature of 20℃, like most of the previous research. The curing time of AAS is 3 days.

3.2.3 Samples preparation

The precursor and activator are mixed together by an IKA mixer for four minutes. The homogenous slurry is then poured into a plastic mold, vibrated for 3 minutes with a compaction table, and sealed with a lid for a specific curing procedure.

3.2.4 Drying procedure

The samples are dried before going through the heat treatment at elevated temperature to reduce the cracking potential and protect the furnace from vapor containing sodium silicate. Different curing procedures are conducted on samples with other purposes. For the samples characterized in terms of crystallization, to limit the drying procedure's effect on the reaction products, the drying process is short and more aggressive. After demolding, samples are taken to the oven and dried at 105℃ for 6 hours. For the samples investigated in terms of integrity and strength, gentler drying procedures are conducted.

For the GP mixtures, after demolding, the samples are put into the oven for drying at 70℃. After 6 hours of drying, one set of samples is brought to heat treatment. Afterward, when the mass of the samples becomes relatively stable at day 3, another set of samples is brought to heat treatment; a final set of samples are then moved to an oven at 105℃ for 1 day to further remove the water and then brought to heat treatment. The properties of these samples are compared to investigate the effect of the drying before heat treatment.

3.2.5 Heat treatment

After the drying procedure, the samples are brought to the furnace for heat treatment at 800℃ with 2 hours of soaking. The heating rate is selected as 2℃/min with the consideration of the time and cracking potential. The samples are placed on alumina rods in order to reduce the cracking potential. As shown in the literature review, the thermal shrinkage of AAMs could be up to 20%. Significant stress can be induced if the AAMs ceramic is externally restrained during heat treatment. In such a case, the cracking potential will be very high. Besides, lifting the sample instead of placing it on the bottom allows the air to flow through the created gap. This measure leads to a smaller temperature difference between the upper and lower surfaces of the sample. Otherwise, the temperature gradient could curve the sample and initiate cracks.

An alumina crucible is placed at the bottom to reduce any risk of unexpected melting of the samples.

3.3 Properties

Some critical characteristics of the samples are investigated to preliminarily estimate the feasibility of fabricating AAMs ceramic tiles with the as-cast method.

The integrity of the samples is investigated by visual observation and photographically recorded after demolding, during/after the drying, and after the heat treatment. A three-point bending test is conducted on the relatively integral mixtures after the heat treatment. For each mixture, four replicates are prepared and tested.

The crystallization of samples is investigated by XRD. Unheated and heated samples are ground into fine powders by hand, followed by immersion in 2-propanol to substitute the water and terminate the reaction. By this method, no significant changes in the structure will be induced [51]. The powder samples are then characterized by X-ray diffractometer (Bruker D8 Advance) with Cu Kα radiation in a range of 10 – 70° (2θ) with a step of 0.04° and a counting time of 2s per step. The samples will be characterized by XRD regardless of the integrity condition after heat treatment. This is with the consideration that the integrity of the samples can be improved by the selection of fabrication method, adjusting the water content, optimizing the drying procedure and heating curve, etc., which can be more thoroughly studied and optimized in the future; but on the other hand, these changes or optimization will not have a considerable impact on its crystallization, and this information from this preliminary research is still valuable for the upcoming research.

4 Results and discussions

4.1 Crystallization

4.1.1 Geopolymer

2.1.1.1 Crystallization of unheated GP sample

XRD patterns of unheated GP samples with different mix proportions are shown in Figure 4.1.1, where the abbreviation -U in the sample name stands for unheated.

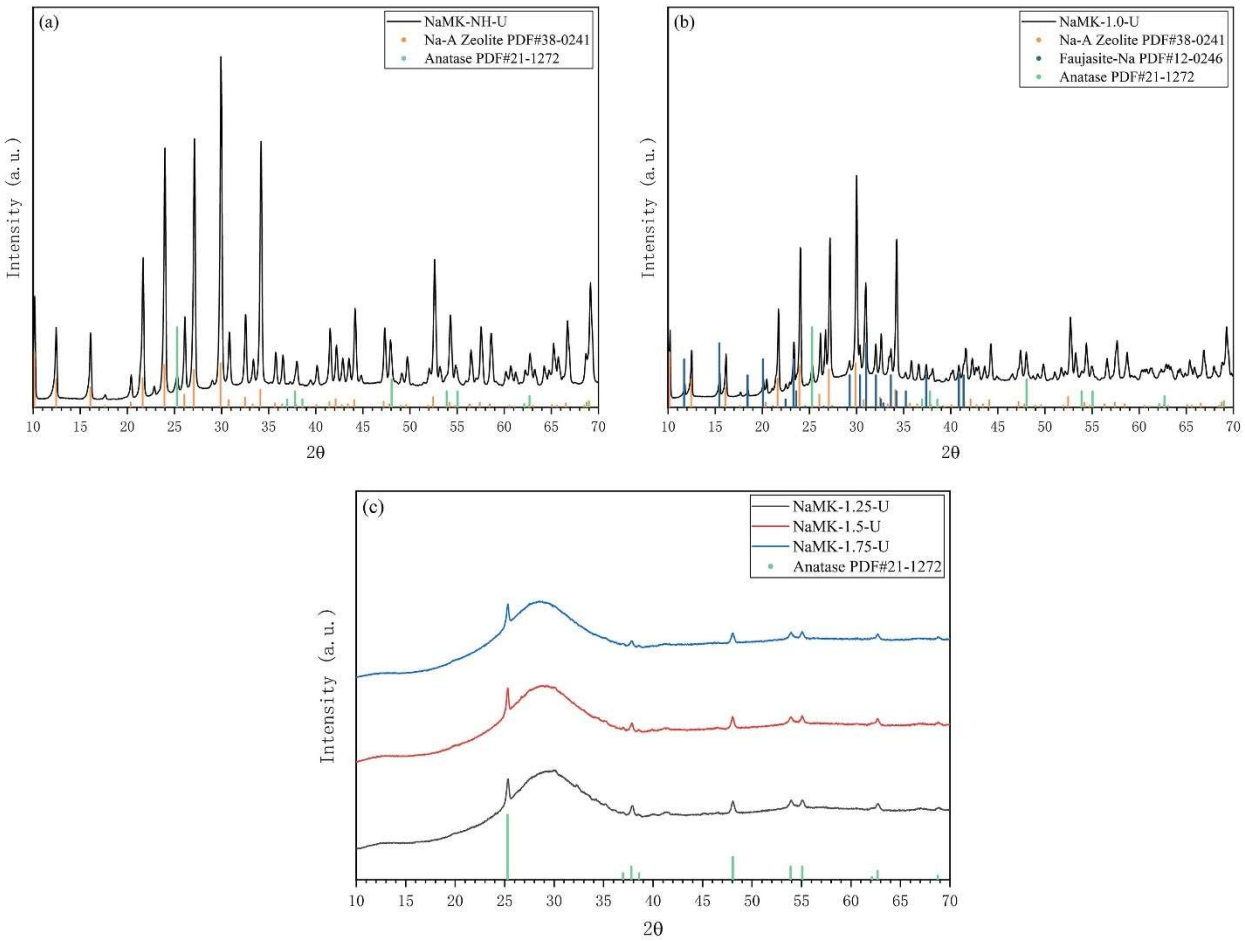

Figure 4.1.1 XRD patterns of the sample before heat treatment: (a) NaMK-NH-U; (b) NaMK-1.0-U; (c) NaMK-(1.25-1.75)-U

Due to the similarity in structure, GP has been widely viewed as the amorphous analog or precursor of zeolite. Zeolites are aluminosilicate solids with a honeycomb framework and are widely used as sorbents and molecular sieves [50]. Zeolite formation in GP was commonly found in the literature [8, 21, 52-54]. This characteristic was also noticed in this study. Crystallization of Na-A zeolite ($Na_2Al_2Si_{1.85}O_{7.7} \cdot 5.1H_2O$) was found in the sodium hydroxide-activated metakaolin (NaMK-NH-U). While for the sodium silicate-activated metakaolin with Si/Al ratio equal to 1 (NaMK-1.0-U), in addition to Na-A zeolite, crystallization of faujasite was also found. The formation of Na-A zeolite is not commonly seen in the literature. Its formation might be attributed to higher water content and curing temperature in this study, which are favorable for Na-A zeolite formation [53]. For the 3-day

curing samples with a higher Si/Al ratio (≥ 1.25), the XRD patterns were very similar and mostly amorphous, as shown in Figure 4.1.1 (c). For all the GP samples, the diffractogram showed a hump centering at 28-30 degrees 2θ. This is a typical characteristic of GP, and the hump is attributed to the main reaction product N-A-S-H gel [39, 55]. In addition, the TiO_2 impurity from metakaolin was also detected in all samples.

A NaMK-1.25 sample was further cured to day 7 (NaMK-1.25-7D-U) to investigate the influence of curing time on the phase composition of the unheated sample. A comparison is shown in Figure 4.1.2 and reveals the considerable effect of curing time. In contrast to the 3-day curing sample, the XRD pattern of the 7-day curing sample showed the formation of Na-A zeolite due to the higher extent of reaction and polymerization.

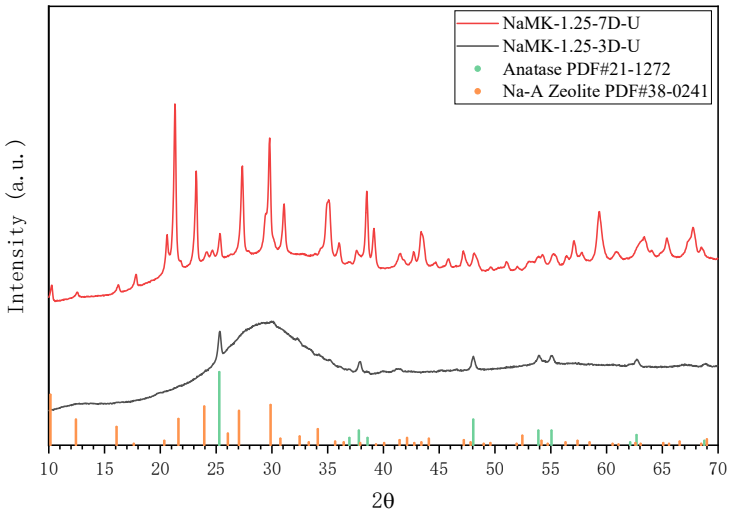

Figure 4.1.2 XRD patterns of NaMK-1.25 sample with different curing times (3 days vs. 7 days)

2.1.1.2 Crystallization of heated GP samples with different mix proportions

Figure 4.1.3 shows the XRD patterns of GP samples with different mix proportions after heat treatment. The zeolites observed in the unheated samples completely decomposed after heating to 800°C. A considerable amount of crystallization was found in the samples with a low Si/Al ratio (≤ 1.25). In contrast, the GP with a higher Si/Al ratio remained mostly amorphous. This trend is in line with observations in the literature. The GP with a higher Si/Al ratio is more resilient to crystallization and has a higher crystallization temperature [34]. The higher Si/Al ratio leads to a higher compositional deviation from the thermodynamically favored crystallization product nepheline ($NaAlSiO_4$) [34, 57, 58] whose Si/Al ratio equals 1. Jadeite ($NaAlSi_2O_6$) is the crystal that is compositionally closer to the samples with a high Si/Al ratio. However, jadeite is only stable at high pressure and, therefore, will not be formed in this case [57]. For these reasons, the higher the Si/Al ratio of the GP is, the more silicon that cannot cooperate into crystalline phase and remains in glass matrix, resulting in a lower extent of crystallization.

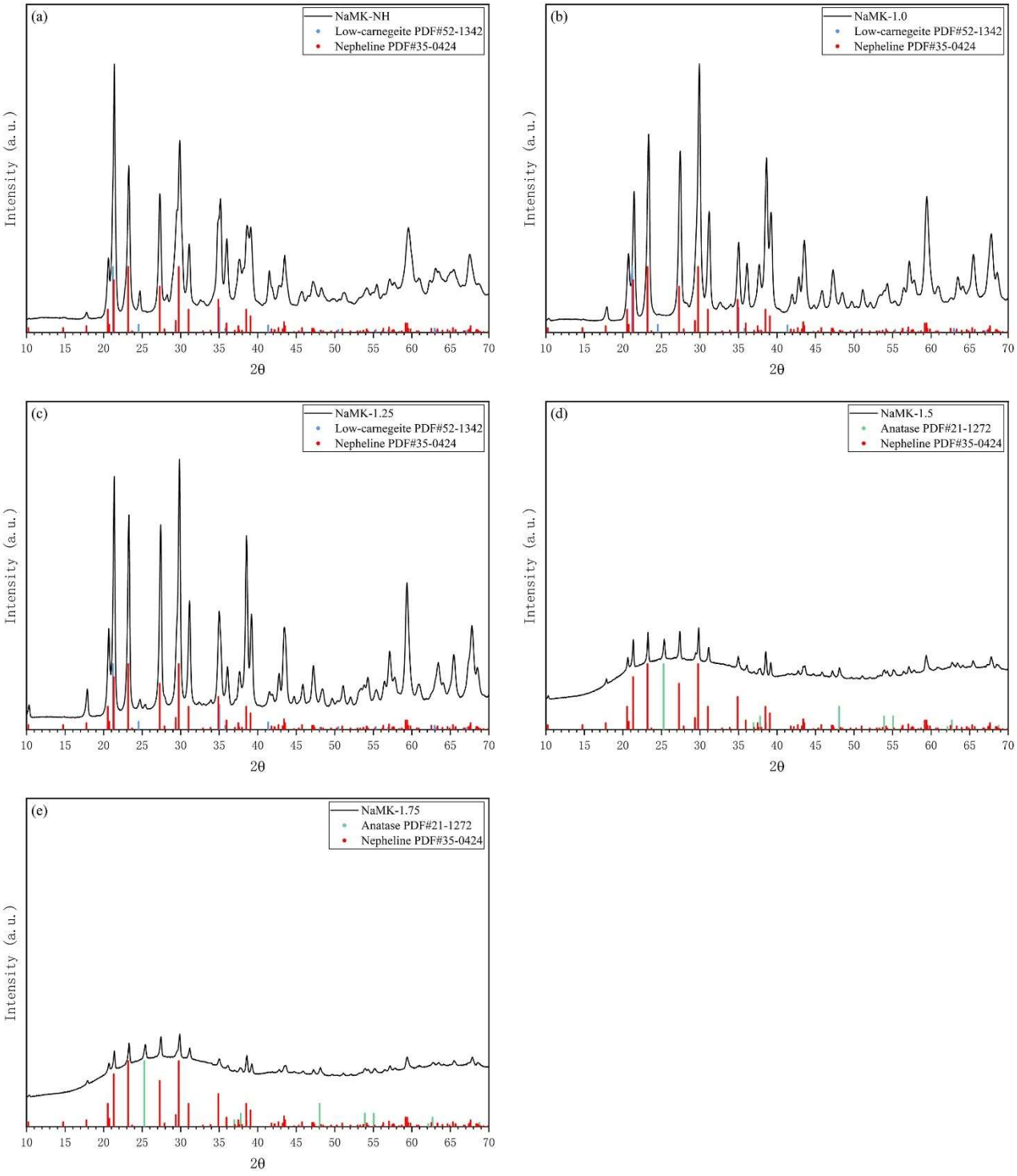

Figure 4.1.3 XRD patterns of the sample with different compositions after heat treatment: (a) NaMK-NH; (b) NaMK-1.0; (c) NaMK-1.25; (d) NaMK-1.5; (E) NaMK-1.75

Crystallization of nepheline can be observed in all specimens after heat treatment. Although only a minor nepheline was found in NaMK-1.5 and NaMK-1.75 in this study, it was reported that a much higher extent of crystallization could be achieved by further increasing the sintering temperature. The crystallization of nepheline is mainly attributed to the disintegration and devitrification of the disordered N-A-S-H gel [33, 58-60]. In addition, Na-A zeolite was found in the green body before heat treatment, and its disintegration and recrystallization might also contribute to the formation of nepheline [61-63].

Low-carnegiete, in polymorph relationship to nepheline, was also found in the crystalline phase of specimens with a low Si/Al ratio. In contrast to the formation of nepheline, the formation of carnegiete was only seldom observed in the literature [64]. The formation of low-carnegiete is unlikely due to the transformation from nepheline or N-A-S-H gel. This is because the transformation temperature for nepheline to carnegiete is usually above 1200°C [65]. Also, if the low-carnegiete was from the transformation of nepheline, it should also be detected in P. Duxson et al. study [33]. The main difference between this study and [33] is the additional Na-A Zeolite in the green body. Therefore, it is suspected that the formation of carnegiete is attributed to the Na-A zeolite. Although no Na-A zeolite was found in the green body of NaMK-1.25, it might form during the drying procedure at 105°C before the heat treatment. During the heating, the structure of Na-A zeolite in the green body collapses into amorphous phase and later reforms into low-carnegiete and nepheline [61, 66, 67].

It is worth mentioning that the temperature of heat treatment is 800°C, slightly lower than the reported temperature (around 800 - 900°C) for the disintegration of Na-A zeolite and recrystallization to low-carnegiete and nepheline [61-63, 65-67]. The lower transformation temperature in this study might be attributed to the presence of additional water vapor during heating due to the evaporation and dehydroxylation of the N-A-S-H gel. The water vapor during the heating can cause the destruction of the zeolite framework by the hydrolytic splitting of Si-O-Al bonds, and cause an up to 300°C reduction in the disintegration and crystallization temperature of Na-A zeolite [68].

2.1.1.3 Crystallization of GP samples with different curing time

The geopolymerization reaction of AAMs takes time. Therefore, the degree of reaction of AAMs is positively related to the curing time. In this study, the crystallization of mixture NaMK-1.25 with 1-day, 3-day, and 7-day curing was investigated.

The crystallization of the green body before heat treatment has already been discussed in section 4.1.1.1. Prolonging the curing leads to not only a higher degree of reaction, but also the formation of a considerable amount of Na-A zeolite. The crystallization of the heated samples NaMK-1.25-(1-7d) was studied by XRD. The XRD patterns are shown individually in Figure 4.1.4 and plotted together in Figure 4.1.5 with color mapping the intensity from purple to red.

The difference in diffractograms shows the considerable influence of curing time and, to a certain extent, demonstrates that the crystallization is the transformation from the reaction products of the geopolymerization, instead of a solid phase reaction between raw materials. All the samples showed identical crystallization products consisting of nepheline and low-carnegiete. Comparing the NaMK-1.25-1d sample with the two longer cured samples, an obvious exclusive hump can be seen on the NaMK-1.25-1d XRD pattern, indicating the remaining high amount of amorphous phase. With longer curing time, the GP has a higher degree of reaction and therefore, more reaction products N-A-S-H gel which later transforms into a crystalline phase. In addition, the synthesis of geopolymer is a process of polycondensation of monomers [8]. With a longer curing time, the reaction of geopolymer is more complete, which might result in a higher degree of polymerization and improve the order of the short-range structure [69]. And the higher degree of short-range order might be favorable for the nucleation and crystallization later [70].

For the comparison between NaMK-1.25-3d and NaMK-1.25-7d samples, the most significant difference was the much higher intensity of the characteristic peaks of low-carnegiete. This is attributed to the formation of Na-A zeolite during the prolonged curing, as discussed in the comparison between the XRD patterns of the green bodies. On the other hand, the difference in nepheline crystallization between 3d and 7d was smaller than the difference between 1d and 3d/7d. This trend conforms to the characteristic of the AAMs reaction progress that most of the reaction finished in the first few days [71, 72].

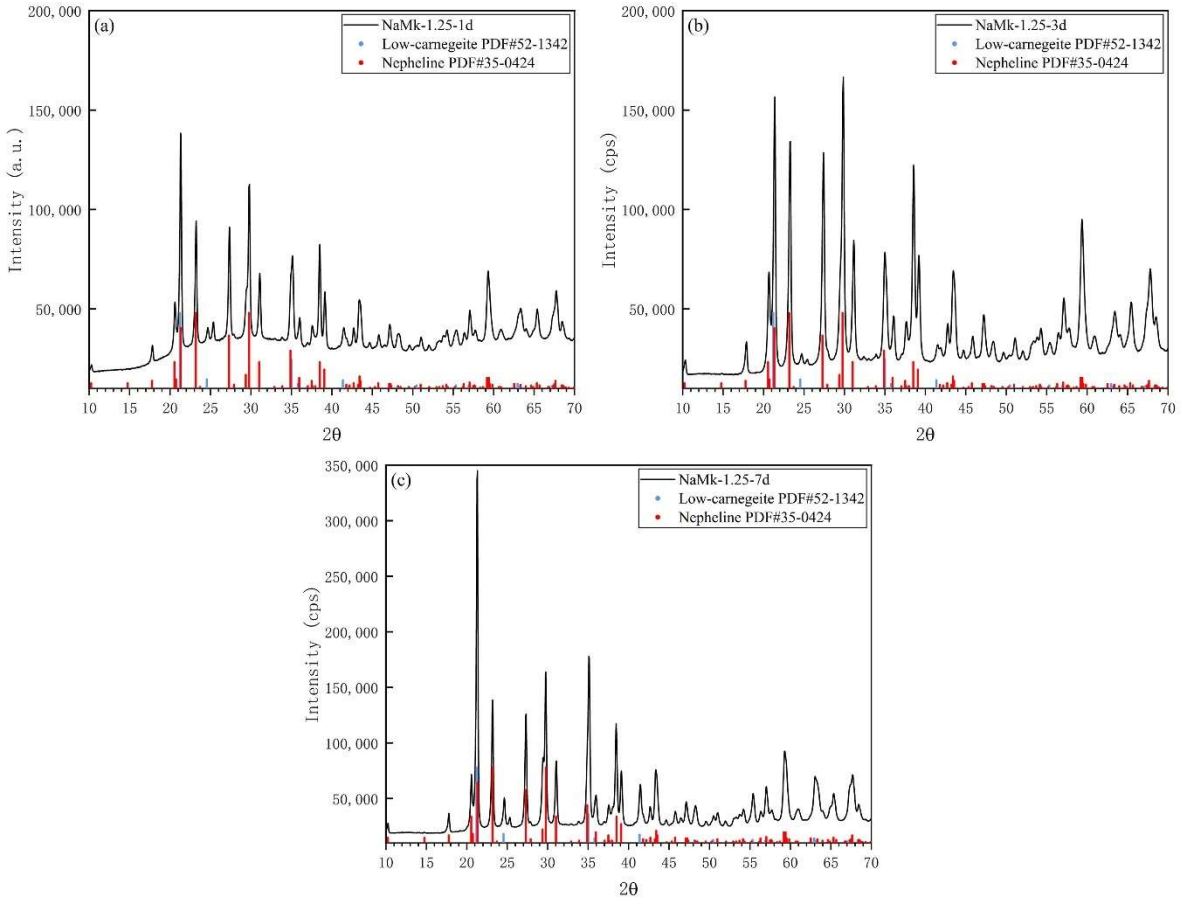

Figure 4.1.4 XRD patterns of NaMK-1.25 samples with different curing lengths: (a) 1 day; (b) 3 days; (c) 7 days

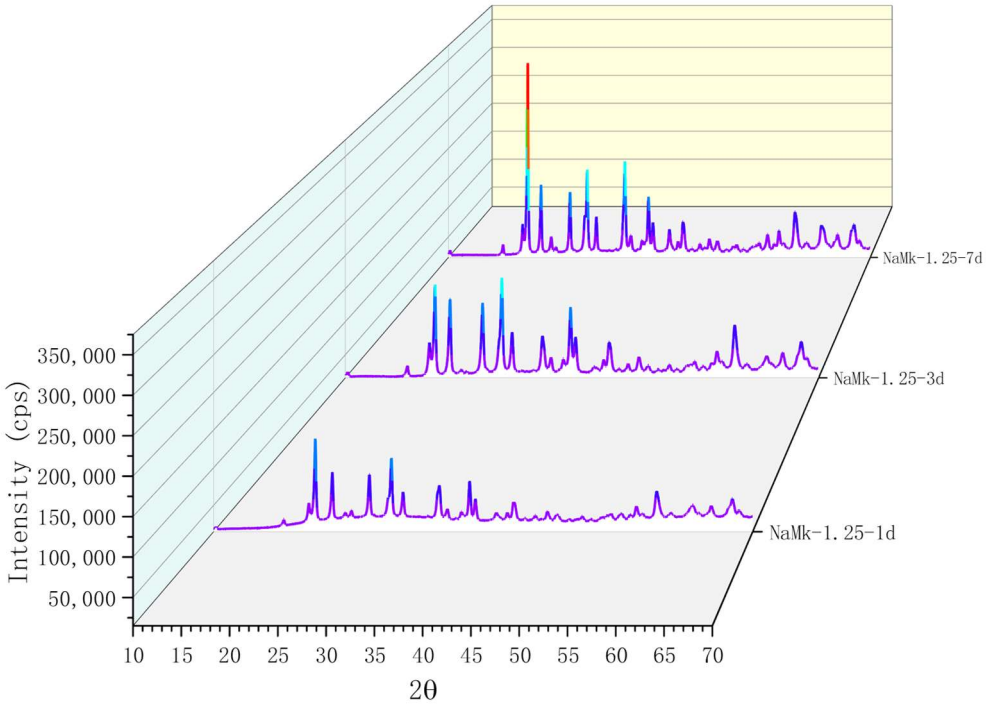

Figure 4.1.5 Comparison between XRD patterns of NaMK-1.25 samples with different curing times, where the magnitude of intensity was mapped by color from purple to red

2.1.1.4 Crystallization of GP samples with different curing temperatures

Curing temperature is another crucial factor that influences the chemical reaction and the microstructure of GP. The curing temperature in literature is highly varied. Crystallization of heated GP samples with curing temperatures of 20℃, 45℃, 70℃, and 95℃ is studied, as shown in Figure 4.1.6.

It can be clearly seen that curing temperature has a considerable influence on the crystallization behavior. Although all the samples gave identical crystallization products after heat treatment, the different extents of crystallization can be clearly recognized by the presence of a hump that belongs to the amorphous phase. The XRD patterns for the sample cured at temperatures other than 70℃ showed clear humps. The XRD patterns of NaMK-1.25-20℃ and NaMK-1.25-45℃ are almost identical. When the temperature increased to 70℃, the extent of crystallization was clearly improved, which might be attributed to a higher degree of reaction and the formation of zeolites. However, when further increased the curing temperature to 95℃, the hump reappeared and was even slightly higher than those at room temperature. The observed trend suggests that an ideal curing temperature leads to the highest extent of crystallization when the curing time is unchanged. The reason behind might be, for the curing temperatures involved in this study, 70℃ led to the higher efficiency of the geopolymeric reaction, as investigated in literature [73]. Therefore, it can be concluded that the ideal curing temperature for synthesis GP ceramic is around 70℃.

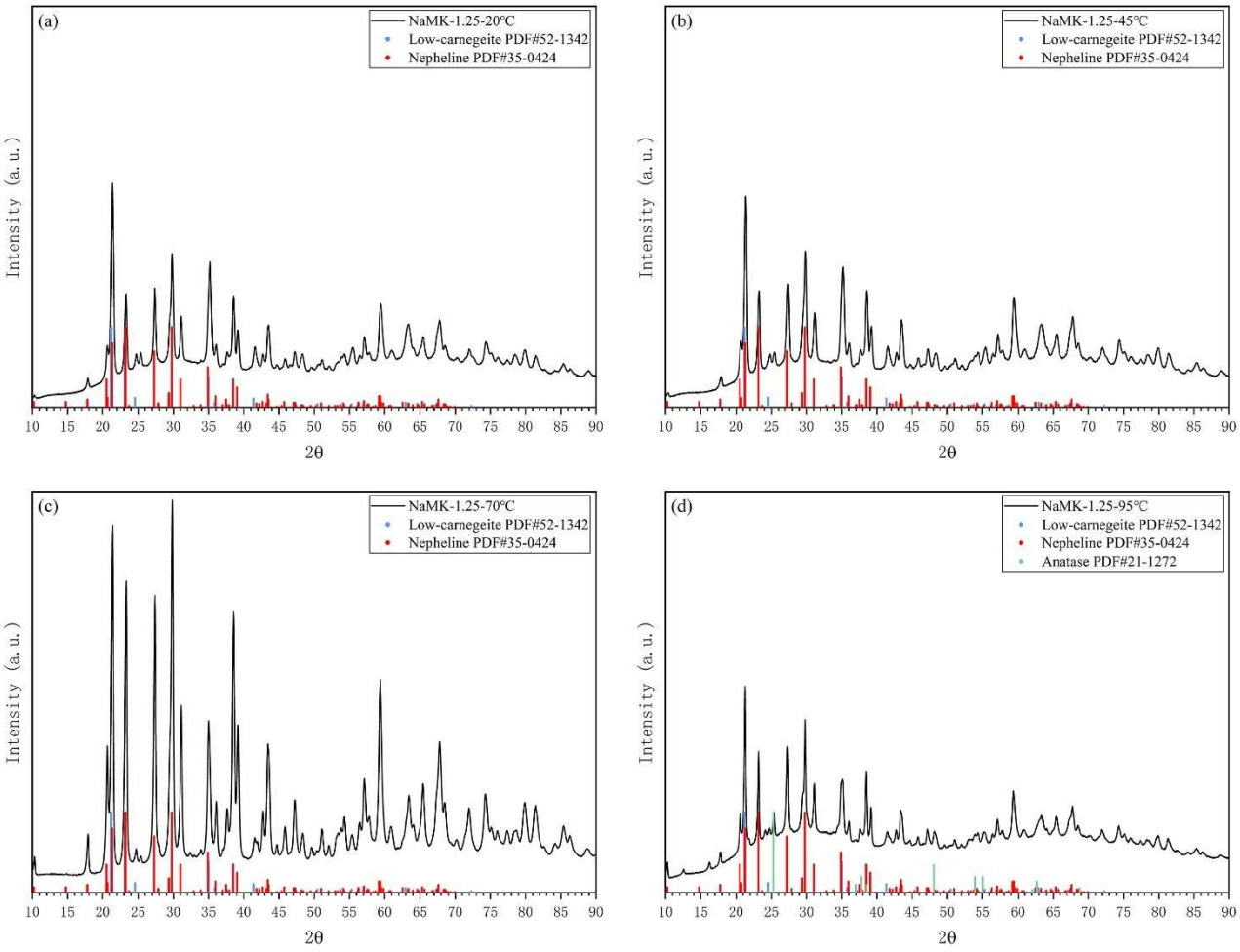

Figure 4.1.6 XRD patterns of NaMK-1.25 samples with different curing temperatures: (a) 20℃, (b) 45℃, (c) 70℃, (d) 95℃

2.1.1.5 Crystallization of GP samples with alternative silica sources

GP mixtures are prepared with the metakaolin and alkali-silicate solution. The samples discussed above are all prepared with the commercial sodium silicate solution. On the other hand, it is possible to use an alternative silica source to further reduce the environmental impact and cost [38]. Rice husk ash (RHA) was used to substitute the silica from the water glass solution in this section, and two mixtures were studied. NaMK-1.25-lRHA stands for the mixture that RHA pre-dissolved in the NaOH solution, while NaMK-1.25-sRHA stands for the mixture that RHA directly added during the mixing. The XRD patterns after heat treatment are shown in Figure 4.1.7.

The results show the feasibility of fabricating GP ceramic with RHA as the silica source. The NaMK-1.25-lRHA show a very comparable extent of crystallization to the samples prepared with commercial sodium silicate solution. Its crystallization products are mostly nepheline. The XRD patterns are closer to NaMK-1.0 rather than NaMK-1.25, which might be attributed to the slower dissolution and lower reactivity of the silicate in the RHA. The composition of the GP is calculated without considering the form of the silicate in the system. In the sodium silicate solution, silicate is solute. Compared to the solute, silicate provided with RHA undoubtedly has slower dissolution and lower reactivity. As a result, the amount of reactive silicate in the NaMK-1.25-lRHA paste is less than the calculated stoichiometry value. Therefore, the actual Si/Al ratio in the NaMK-1.25-lRHA is actually lower than the calculated value of 1.25, and the resultant diffractogram is closer to NaMK-1.0. The XRD pattern of NaMK-1.25-sRHA is less favorable, and it might be due to the lower dissolution and extent of reaction.

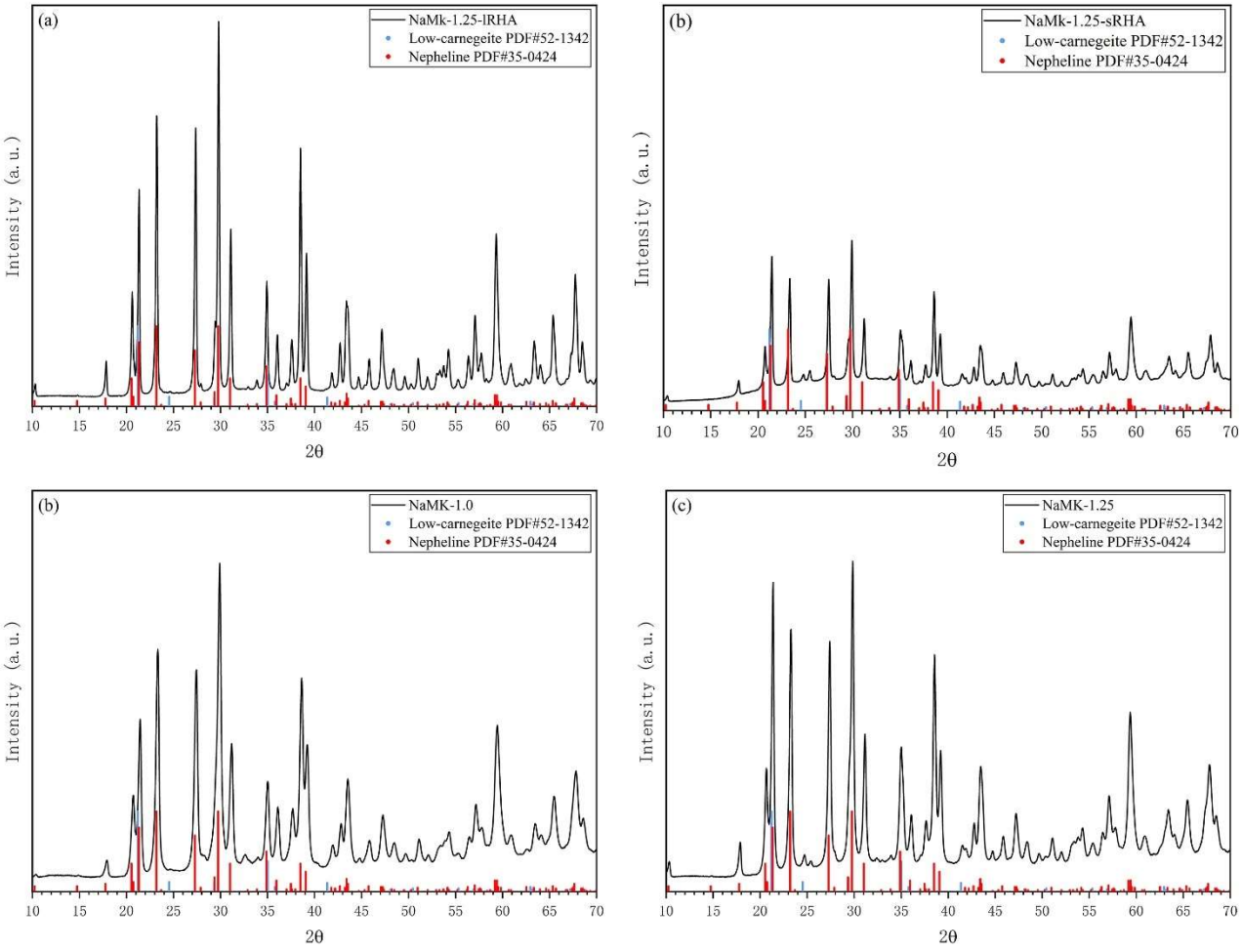

Figure 4.1.6 XRD patterns of GP samples using RHA and NaOH: (a) NaMK-1.25-lRHA, (b) NaMK-1.25-sRHA, or commercial sodium silicate solution: (c) NaMK-1.0, (d) NaMK-1.25

4.1.2 Alkali-activated slag

Crystallization of unheated and heated AAS with the composition of NaS-*Ms*-*N/B* was studied by XRD. Figure 4.1.7 shows the XRD patterns of 3-day AAS samples before the heat treatment. The patterns are very similar, especially for the sodium silicate-activated slag samples (i.e., Ms＞0). For all the samples, the presence of a small broad peak at approximately 29° is a characteristic of AAS, and it is attributed to the disordered reaction products C-(A)-S-H [27, 37, 38, 74-76]. The slag activated by sodium hydroxide (NaS-0-4%) has a slightly sharper peak, which might be due to the formation of a poorly crystalline C-A-S-H phase that has some structure similarity with the tobermorite group [75, 76]. In addition, hydrotalcite is also observed in the NaS-0-4% samples, which is commonly seen in slag with a high magnesium content.

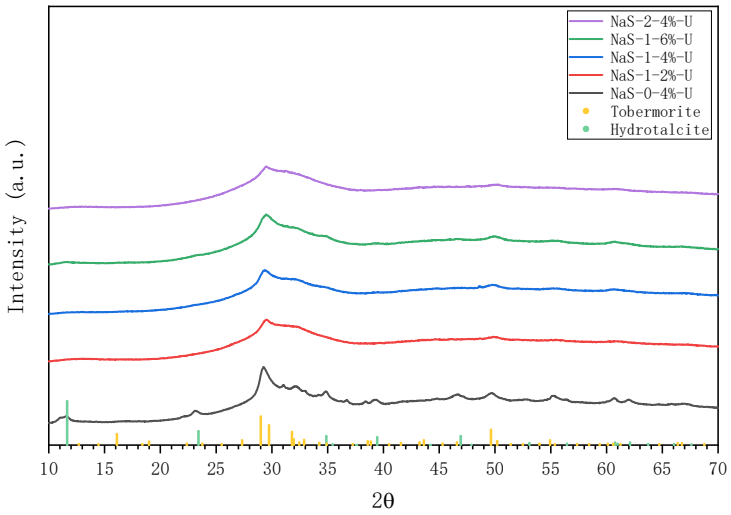

Figure 4.1.7 XRD patterns of unheated AAS samples

Figure 4.1.8 shows the XRD patterns of AAS samples after heat treatment. The crystalline products of the samples are similar, but the patterns are considerably dependent on the mix proportion.

All samples showed a considerable extent of crystallization, except for the NaS-1-2%, which shows a clear remaining hump. Comparatively, the difference between NaS-1-4% and NaS-1-6% is much smaller. Compared to the unheated green body shown in Figure 4.1.7, the remaining hump of heated NaS-1-2% shifted to the right at around 31°, corresponding to the hump of unreacted slag. Alkali content of 2% is usually the lower limit of the suggested AAS mix design [77]. It is generally accepted that the lower alkali dosage leads to lower alkalinity of the activator, and in this case, the curing time is short (3 days) [77, 78]. As a result, 2% alkali content led to a lower reaction rate and a lower reaction degree of slag. Therefore, after heat treatment, the hump of unreacted slag can be observed from XRD patterns. In case of enough alkali, the unreacted slag is not detected in the heated samples. The influence of excessive alkali in the 6% mixture did not have much influence, which agrees with the observation in the literature [27]. From another perspective, this observation also indicates that the crystallization products are derived from the reaction products instead of the unreacted raw material slag. And this emphasizes the contribution and significance of the geopolymerization reaction prior to the heat treatment.

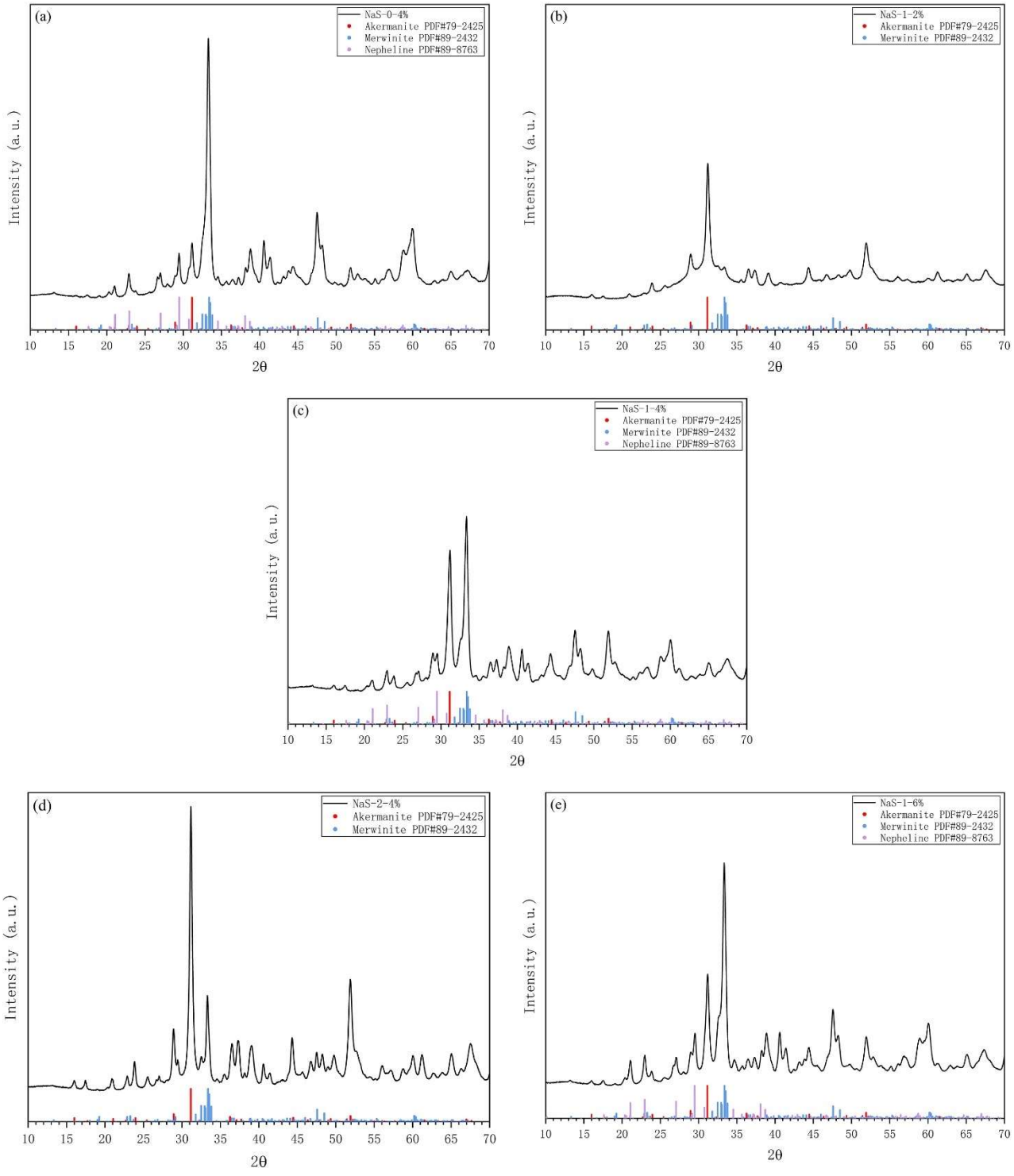

Figure 4.1.8 XRD patterns of AAS samples after heat treatment: (a) NaS-0-4%; (b) NaS-1-2%; (c) NaS-1-4%; (d) NaS-2-4%; (e) NaS-1-6%.

Depending on the mix proportions, the dominant crystalline phase after heat treatment is found to be the akermanite ($Ca_2Mg[Si_2O_7]$) and/or merwinite ($Ca_3Mg(SiO_4)_2$), in agreement with the findings in the literature. However, the possibility of the presence of gehlenite ($Ca_2Al[AlSiO_7]$) cannot be foreclosed. The diffractogram of akermanite and gehlenite are very similar because they are isomorphic, and there might be an aluminium substitution for magnesium or silica [37, 79, 80]. The formation of the merwinite is likely to be the reaction between the decomposition products of C-(A)-S-H and the magnesium phase in the slag. By comparing the XRD patterns of NaS-(0-2)-4% samples,

it can be observed that with increasing Ms (i.e., higher Si environment), the intensity of the characteristic peak of akermanite increases while the peak of merwinite decreases, implying that the formation of akermanite might be the further reaction of transition compounds merwinite with magnesium and silicate phase in the high-Si environment [81]. The hardness of akermanite is considerably higher than merwinite. To fabricate ceramic tiles, a higher Ms might be more favorable.

Additionally, a nepheline-like minority was also found in some samples, which might be due to the decomposition and recrystallization of N-A-S-H gel, as discussed in the GP section.

4.2 Integrity

There is no doubt that a qualified ceramic tile product should be intact and without any crack. However, AAMs may show considerable cracking potential when applied in construction, especially when subjected to drying and restraint. Some preliminary research on fabricating ceramic from as-cast AAMs has also reported the cracking issue. Drying is inevitable when fabricating AAMs ceramic tiles. Therefore, it could be inferred that cracking is a very challenging issue when fabricating AAMs ceramic tiles. On the other hand, though there is a high cracking potential, cracks might also be healed by the considerable shrinking during the heat treatment.

In this section, the integrity of the samples after drying or heat treatment is shown and qualitatively compared. Potential solutions are also proposed to improve the integrity.

4.2.1 The integrity of geopolymer samples

The drying procedure was conducted on the GP samples before the heat treatment, which is a conventional procedure in the ceramic fabrication industry to reduce the cracking potential. The condition of samples with different compositions (varying Si/Al ratio) after 6 hours of drying at 70℃, 3 days of drying at 70℃, and 1 day of further drying at 105℃ were investigated before the heat treatment, as shown in Figure 4.2.1. The samples with lower water content ($H_2O/Na_2O = 9$, 11, NaMK-1.25-(9,11)w) were also investigated. Because of the unacceptable workability, NaMK-1.25-9w was abandoned.

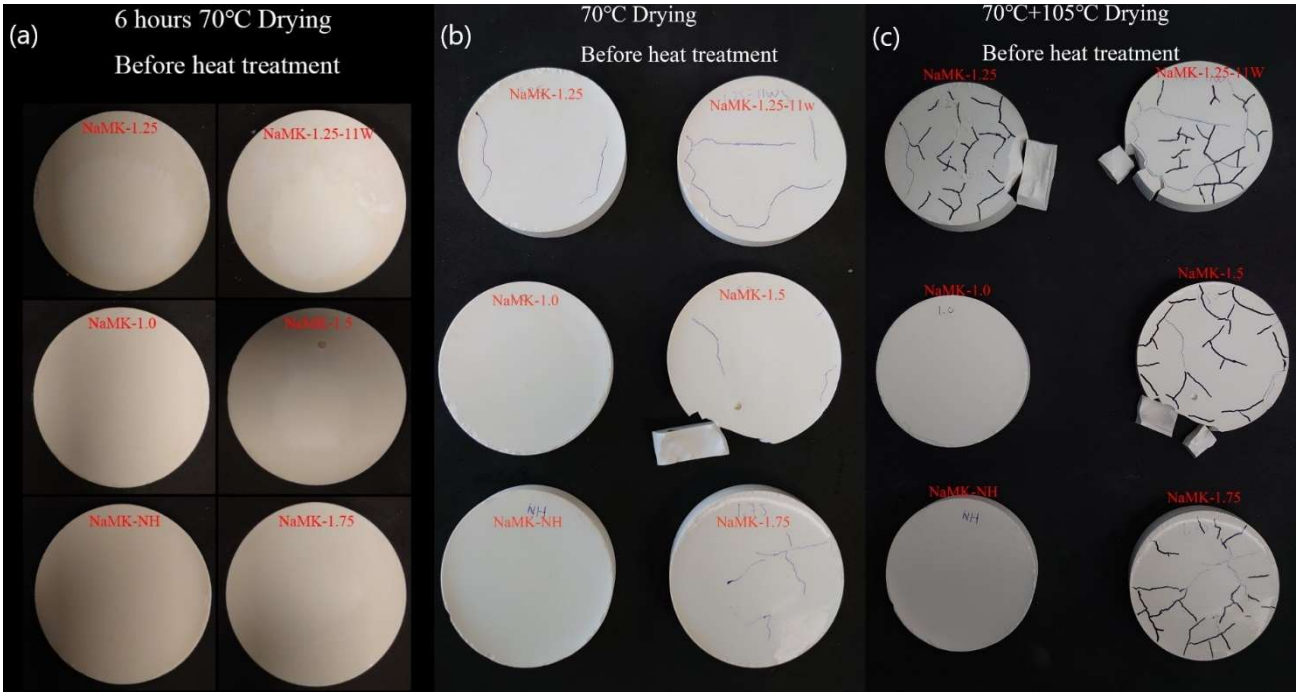

Figure 4.2.1 Samples condition (a) after drying for 6 hours at 70℃; (b) reached relative stable mass at 70℃ on day 3; and (c) further at 105℃ for 1 day. Cracks are indicated by drawing lines. The fine blue lines referred to the cracks observed at 70℃, and the thick black line referred to cracks newly found after drying at 105℃

After drying, these three sets of samples were brought to heat treatment. The samples' condition after heat treatment is documented and shown in Figure 4.2.2.

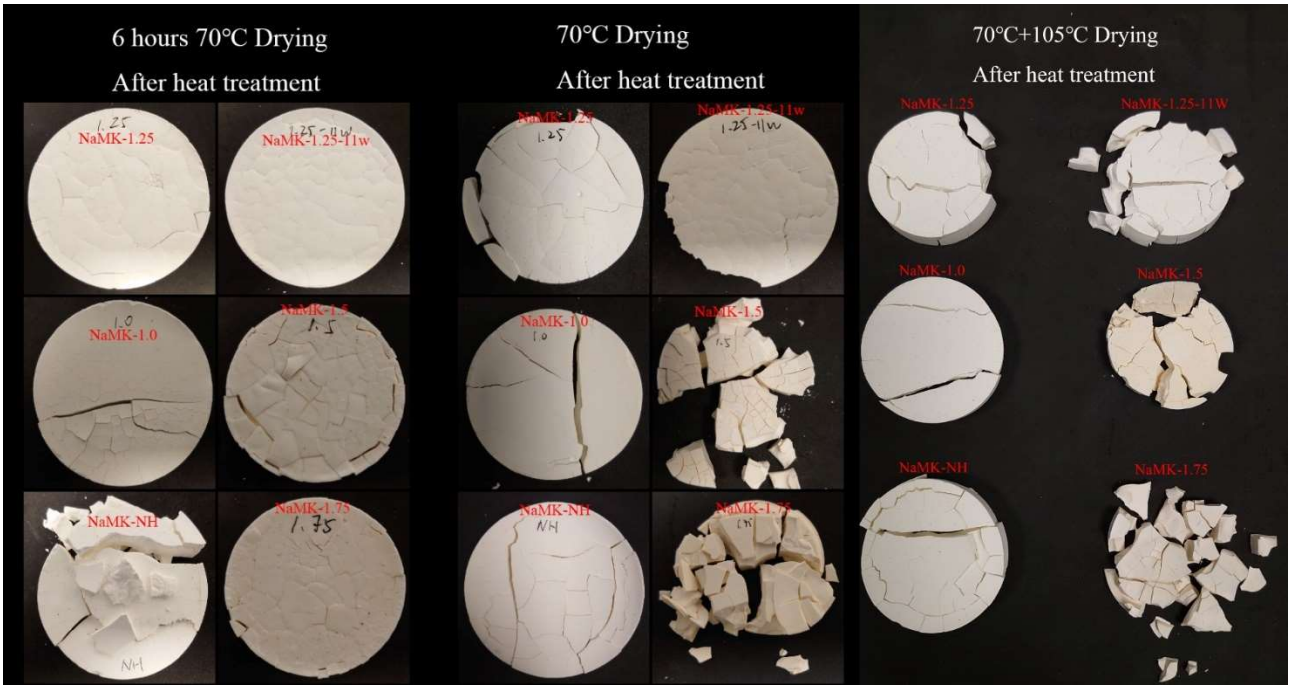

Figure 4.2.2 Samples condition after heat treatment: (a) drying for 6 hours at 70℃; (b) drying until relatively stable mass at 70℃; and (c) further drying at 105℃ for 1 day.

Two kinds of cracking patterns can be observed on the samples, one is the map cracking, and the other is the main crack. Map cracking is the fine cracks on the surface that formulate a network, while the main crack is the wide crack that could run through the samples. The main crack is unlikely caused by the external restraint because the special effort was taken to reduce the external restrain during the drying and heat treatment, as mentioned above. Therefore, it is believed that the main crack is the result of the propagation and connection of the fine cracks [12].

Figure 4.2.1 shows the samples' condition after drying with specific programs. After 6 hours of drying at 70°C, no initiation of cracks was observed on the specimen, regardless of the composition. When further drying the samples at 70°C until reaching a relative stable mass on day 3, several cracks can be observed on the specimens with Si/Al ratio ≥ 1.25. It was also observed that parts of the sample NaMK-1.5 have already spalled off. This indicates that, after drying to constant mass at 70°C, some cracks might have already deeply penetrated into the sample, bridged together, and formed a through crack along the thickness direction. When the samples were further dried at 105°C, samples NaMK-NH and NaMK-1.0 remained intact, and no sign of crack initiation was found. On the other hand, a typical map cracking pattern was found for the specimen with Si/Al ratio ⩾ 1.25 due to the initiation of new cracks and the development of existing cracks.

As shown in Figure 4.2.2, none of the samples remained satisfactory integrity after the heat treatment. The cracking characteristic is found to be highly dependent on the composition of the samples. The cracking issue gets more serious with a higher Si/Al ratio. After the heat treatment, the samples with a lower Si/Al ratio broke into two or three large pieces, while the samples with Si/Al ratio higher than 1.5 broke into countless pieces. The tendency to form a map cracking also increases with the increasing Si/Al ratio. For the samples NaMK-NH and NaMK-1.0, several main cracks were formed, with only a slight extent of map cracking; for the sample NaMK-1.25, obvious gridding can be found on the surface, while for the NaMK-1.5 and NaMK-1.75, the map cracking had smaller grids, penetrated, and broke the samples into pieces. No considerable difference can be observed for the sample with lower water content.

The cracking is attributed to the water in the samples. Because of the platelike structure, high surface area, and high electrostatic charge density of the metakaolin particles, producing GP with metakaolin usually requires a relatively large amount of water that usually results in a w/b around 0.7 [82]. On the other hand, unlike the hydration of the OPC, during the synthesis of AAMs, the water has little contribution to the chemical reaction and is not incorporated directly into the gel structure and evaporated during the heating [83, 84]. When the water evaporates from the small pores in the porous AAMs matrix, capillary force is created as a result of the formation of the meniscus at the vapor/liquid interface [85]. The liquid is then subjected to tension and creates compression in the matrix, which accounts for the shrinkage observed in stage II revealed form the dilatometry test, as indicated in Figure 2,3 [10, 11, 13, 22, 85]. The shrinkage and cracking caused by this capillary action have already been widely studied in gel or cementitious materials. The behavior is highly dependent on the characteristic of the pore structure. The magnitude of the capillary force that can be induced in the matrix is inversely proportional to the pore radius. With finer pore size distribution, the higher maximum capillary force during drying can be created [13, 85, 86]. Meanwhile, the pressure gradient is created along the cross-section due to uneven drying. Similarly, this gradient is also highly dependent on the pore structure. With finer pore size distribution, the matrix has a lower permeability, and the liquid is more difficult to draw from the inside of the matrix, therefore resulting in a larger pressure gradient along the thickness of the matrix, so as the strain. This capillary action is analogous to the thermal gradient and results in cracking at the surface [86].

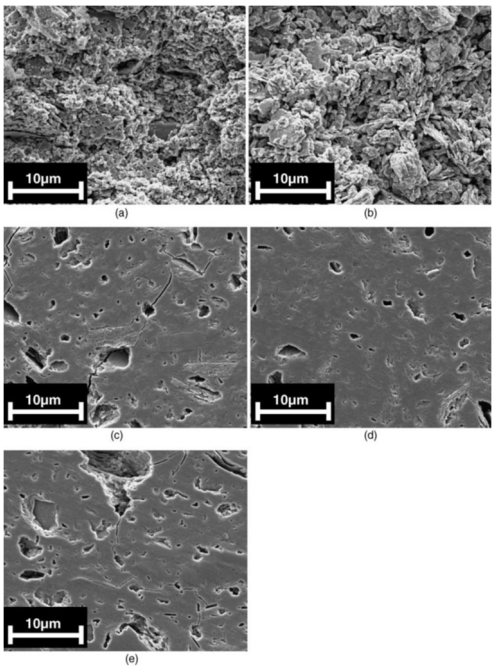

Fig. 4.2.3 SEM micrographs of Na-geopolymers: Si/Al ratio of (a) 1.15, (b) 1.40, (c) 1.65, (d) 1.90 and (e) 2.15 [31]

The difference in cracking tendency observed in varying Si/Al ratios can be explained by the relationship between pore and capillary stress. The microstructure of GP also highly depends on the Si/Al ratio. As shown in Figure 4.2.3, P. Duxson et al. revealed that [31], the GP with a low Si/Al ratio has a porous microstructure comprising clustered dense particulates with large, interconnected pores, while GP with a high Si/Al ratio equal to has a much more homogenous microstructure with much smaller independent pores. The nitrogen adsorption test also showed that the pore size significantly decreases with increasing Si/Al ratio, where the mean pore diameter of the Si/Al 1.15 sample is more than five times larger than the Si/Al 2.15 sample. As explained above, the larger, highly connected pores system in low Si/Al ratio GP will result in lower capillary stress and more even stress distribution, significantly improving the integrity after drying and heat treatment.

Another potential driving force behind the cracking is the vapor pressure that might be created during heat treatment. When subjected to elevated temperature, spalling of the cementitious materials caused by vapor pressure is a well-known deterioration in fire engineering. The evaporation of water in the pores creates a high water vapor pressure on the matrix, which might exceed the matrix tensile capacity and generate cracks [87-89]. Under this criterion, the pores that connect the surface and the internal matrix can be the evacuation path for the water vapor. Therefore, similar to the case of capillary pressure, the more porous the sample, the higher resistance to the vapor pressure under elevated temperature. With much higher porosity and permeability, the low Si/Al ratio samples allow the water vapor release and limit the vapor pressure. In contrast, the high Si/Al ratio samples have a much denser matrix and clogs the water vapor in the matrix, likely resulting in significant cracking and spalling during heat treatment.

An interesting observation is the effect of the drying procedure. For the samples with lower Si/Al ratio, the drying procedure seems to reduce the cracking extent. NaMK-1.0 sample with 6 hours drying procedure exhibited main cracks as well as map cracking; when the mixture was dried at 70℃ for 3 days, the extent of map cracking was considerably reduced; after further dried at 105℃ for 1 day, the samples only had two main cracks. In contrast, for samples with high Si/Al samples, the drying procedure seems to exaggerate the cracking extent. For mixture NaMK-1.5 and NaMK-1.75, though the surface is full of map cracking, the samples with 6 hours drying at 70℃ remained in one piece after heat treatment. However, when subjected to longer drying at 70℃ or 105℃, the samples exhibited much deeper penetrated cracks and were broken into countless pieces. Therefore, for the samples with a high Si/Al ratio, it seems that drying did not necessarily reduce the cracking tendency. This interesting phenomenon is attributed to the cracking condition before heat treatment and the sintering in heat treatment. For the samples remaining integral after drying, i.e., the low Si/Al ratio mixtures, the drying procedure did not create drying cracks at the drying stage and limited the capillary force or vapor pressure created in the heat treatment by reducing the water content in the samples. Therefore, the cracking extent is reduced by the drying procedure. On the other hand, for the samples with a high Si/Al ratio, the cracking had already happened during the drying procedure, and the longer drying procedure allowed the crack further to initiate, widen, connect, and penetrate in the samples. During the heat treatment, vicious sintering at elevated temperatures can eliminate the fine cracks [10, 12, 13]. However, the viscous sintering is not capable of recovering the wide cracks. Instead, the significant shrinkage caused by sintering might even further widen the existing main cracks and result in fully disassembled products [12], which is the case of high Si/Al ratio samples with a longer drying procedure. Therefore, the drying procedure can be both beneficial and harmful to the resultant integrity. If the samples can remain relatively integral after drying, the drying procedure can limit the cracking tendency in the heat treatment, and fine cracks can be recovered by vicious sintering; if wide cracks are already created as a result of drying, they are irrecoverable and might further develop and fully disassemble the samples.

The effect of curing time on the resultant integrity was investigated. A longer curing time (7 days) was applied to one batch of the GP samples. After the curing, the samples are subjected to a drying procedure consisting of 70℃ for 3 days and 105℃ for 1 day. The samples' condition after heat treatment is shown in Figure 4.2.4.

Figure 4.2.4 Comparison on integrity after heat treatment of samples with 3 days curing (left) and 7 days curing (right)

The results showed that longer curing time leads to better integrity. For the low Si/Al ratio samples, the number of cracks was reduced; while for the high Si/Al ratio samples, the samples remained in one piece instead of breaking into pieces. The longer curing time has several contributions to this improvement. First, the longer curing time resulted in a higher degree of reaction and, therefore, higher matrix tensile capacity when the samples were exposed to capillary action and vapor pressure. Besides, the longer curing time also allows the GP to have a more homogenous pore structure along the depth of the samples when exposed to capillary action [90]. When the samples were exposed to a dry environment, the loss of free water around the sample surface was quicker than in the sample core. The difference in drying speed created a different reaction extent during the drying and therefore a difference in pore structure [90]. The longer curing time reduced the microstructure difference between the surface and core, and therefore reduced the capillary stress gradient which generated the cracks [90, 91].

Although the integrity of the products was improved in this case, it is possible that longer curing time might be unfavorable to the sample's integrity. Besides the stronger matrix, the higher degree of reaction will also result in a finer pore structure in the samples. As mentioned above, the magnitude of the capillary force is inversely proportional to the pore size. This should also be taken into account. As a result, when only considering the integrity, there might be a pessimum effect, and the curing time should not be too long or too short.

In addition to the integrity, it should also be remembered that the crystallization considerably depends on the curing time. And the curing time should be long enough to have the desired amount of reaction products that crystallize during heat treatment. Therefore, an optimization of curing time might be needed for different mix proportions.

4.2.2 The integrity of alkali-activated slag samples

In this section, the integrity of AAS samples is discussed. The cured AAS samples with varying mix proportions went through a gentler drying procedure at 40℃ for 3 days before heat treatment. Samples conditions after drying at 40℃ for 2 hours, 40℃ for 3 days, and after heat treatment are shown in Figure 4.2.5. The mix proportion of the sample NaS-*Ms-N/B* is indicated by two numbers marked on

the surface: the first number stands for the *Ms*; the second number in percentage stands for the alkali content *N/B ratio*.

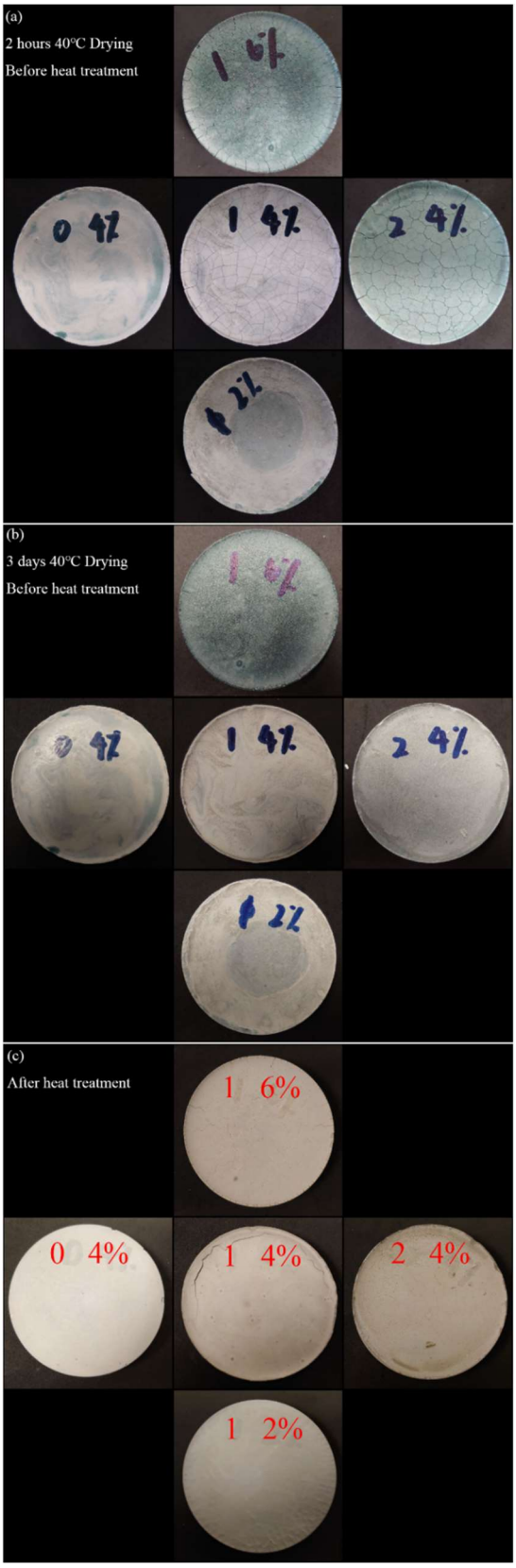

Figure 4.2.5 AAS Samples condition after: (a) drying for 2 hours at 40℃; (b) drying until relative stable mass (~3 days) at 40℃; and (c) heat treatment. Samples were marked with two values: the first one indicates the Ms of the mixture; the second one in percentage indicates the alkali content

During the drying procedure, AAS samples show considerable cracking potential and shrinkage, which conform to the findings in the literature [86, 92-94]. After drying for 2 hours, as shown in Figure 4.2.5 (a), obvious surface map cracking can already be seen on the NaS-1-4%, NaS-1-6%, and NaS-2-4% samples. When the samples continuously dried for 3 days, as shown in Figure 4.2.5 (b), due to the high shrinkage of the specimen, the crack width significantly reduced and became almost invisible from photos. However, the cracks were not healed and still existed.

After the heat treatment, as shown in Figure 4.2.5 (c), the AAS samples showed much better integrity than the GP samples. NaS-0-4% and NaS-1-2% samples remained intact and showed no visible cracking on the surface. However, the texture was visible on the surface of these two samples, indicating cracking during heating but recovered later by the sintering. This is more obvious after grinding out the surface layer of the sample, as indicated in Figure 4.2.6. Only slight cracking was observed for the samples with higher Ms and N/B ratios, and the samples remained in one piece.

Figure 4.2.6 Ground surface of NaS-1-2% sample after heat treatment

Therefore, another batch of samples in the range of NaS-(0~1)-(2~4%) was investigated. The sample condition before and after heat treatment is shown in Figure 4.2.7.

As shown in Figure 4.2.7 (a), the samples showed relatively satisfactory integrity after the drying procedure, except for the NaS-1-3%, which had one main crack. However, the texture is obvious on all the samples, indicating the existence of very tiny but developed cracking.

After heat treatment, as shown in Figure 4.2.7 (b), sample NaS-1-3%, NaS-0.5-3%, and NaS-0.5-2% all showed one main crack on the surface, while the NaS-0-4% and NaS-1-2% sample still remained relatively surface intact.

Similar to GP, the driving force behind the cracking of AAS is attributed to capillary pressure and potential vapor pressure at the elevated temperature. By comparison of the integrity of different AAS samples, it can be observed that the extent of cracking increases with increasing the Ms and N/B ratios. Similar to the effect of increasing the Si/Al ratio in GP, increasing Ms and N/B ratio in AAS also results in a denser microstructure in the AAS samples [27, 78]. The denser microstructure results in higher capillary pressure and pressure gradient in the matrix and generates cracks when the matrix tensile capacity is exceeded.

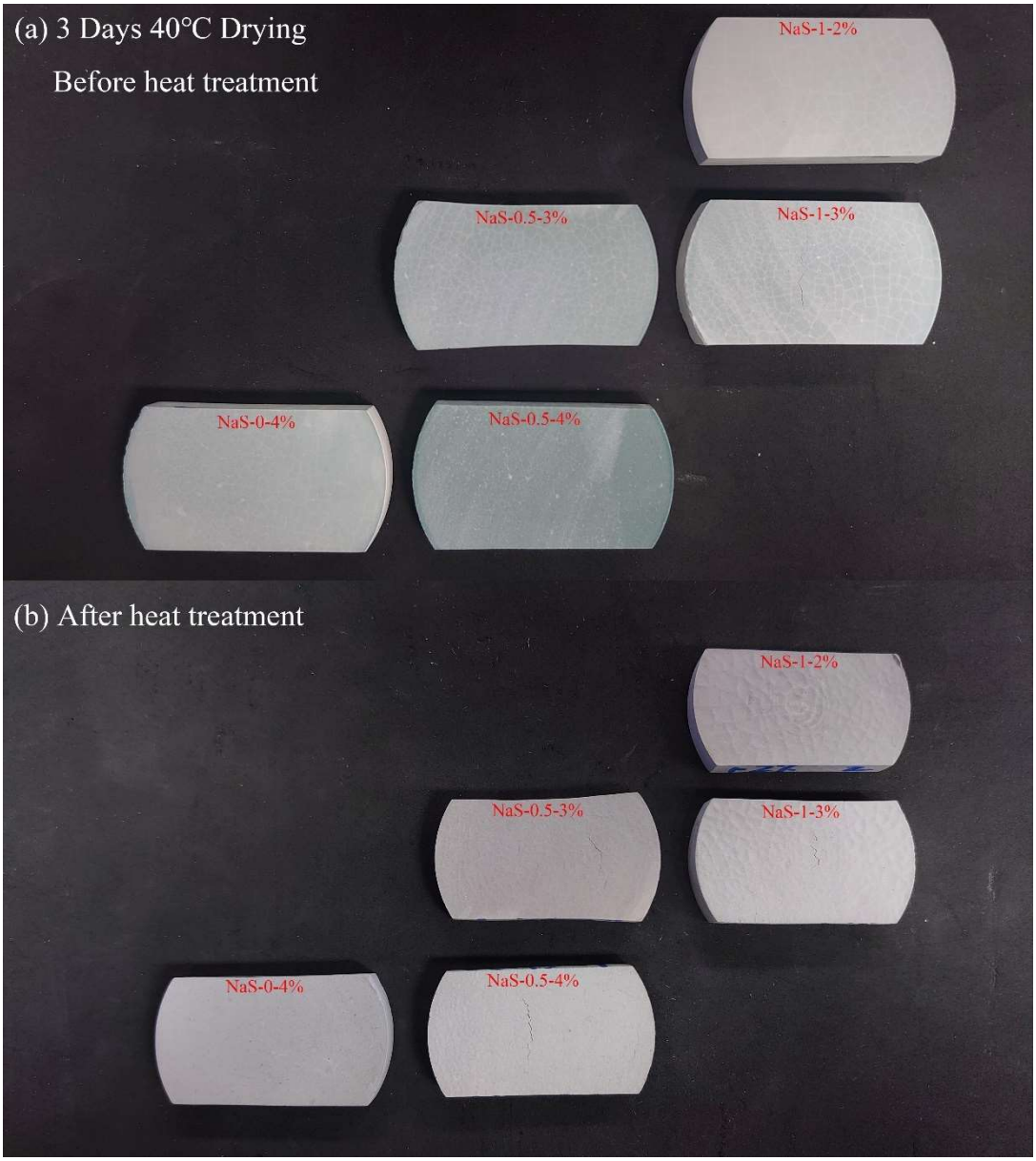

Figure 4.2.7 AAS Samples condition (a) before heat treatment; (b) after heat treatment. Samples were marked with two values: the first one indicates the Ms of the mixture; the second one in percentage indicates the N/B ratio

4.2.3 Improving the integrity

As discussed above, the integrity of the heat-treated as-cast AAMs samples seems to be problematic. Therefore, several attempts were made to improve the integrity.

4.2.4 Prolonging curing time

As shown in section 4.2.1, the integrity of GP ceramic was improved when the curing time was extended to 7 days. By prolonging the curing time, the GP ceramic has a higher resistance to the generated stress when exposed to drying and heat treatment. Besides, with the longer curing, the GP green body has a more homogenous pore structure along the depth after drying [90]. With the more homogenous pore structure, the capillary stress gradient is reduced, so as the cracking potential [90, 91]. However, the effect of drying seems to be a competition between the benefits mentioned above

and the decreasing pore radius. It could be the case that longer curing leads to poorer integrity due to the higher capillary pressure created by finer pore structures.

4.2.5 Addition of sand

C. Kuenzel et al. [42] reported the synthesis of nepheline/quartz ceramic from GP with good integrity. However, the curing time used in their study is so long (77 days) that it is unrealistic for real industrial applications. Nevertheless, the addition of sand does have the effect of restraining the deformation of the paste. By such, the shrinkage difference between the external part and internal part is redudeced, so as the cracking potential. Therefore, the integrity of samples with sand addition was investigated.

The integrity of GP samples with the addition of sand was investigated. The sand used in the study is the commercial standard fine sand in the range of 125-250 um. The amount of additive sand is equal to the mass of the GP. The GP mortar samples were cured for 3 days and dried at 70℃ for 3 days and 105℃ for 1 day before heat treatment.

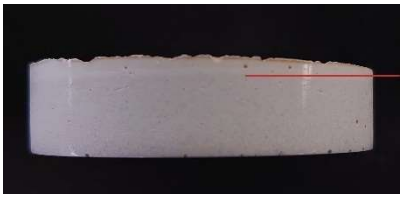

Figure 4.2.8 Lateral view of GP mortar sample before heat treatment. Segregation is indicated by the red line.

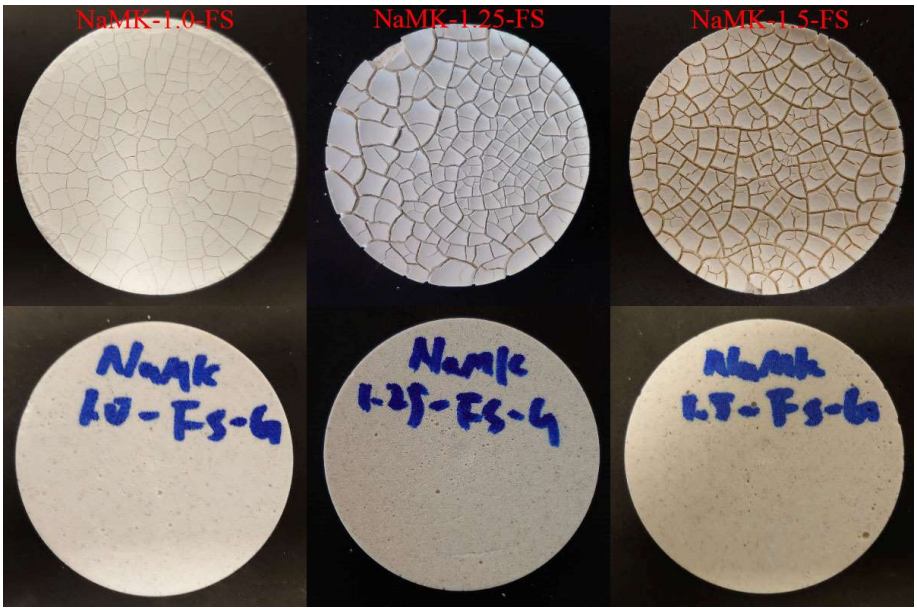

Figure 4.2.9 Samples condition of the upper surface (on top) and bottom surface (on bottom) after the heat treatment.

When sand is incorporated, the segregation of sand can be a problem. The typical lateral view of the samples with sand is shown in Figure 4.2.8. Segregation can be found on the specimen. Segregation played a crucial role in the subsequent heat treatment.

The samples' condition after heat treatment is shown in Figure 4.2.9. A clear difference condition can be observed between different layers. The bottom layer was in good integrity with the help of sand. But for the surface layer, which majorly consists of GP paste, the cracking extent was worse than before. This is due to the difference in thermal shrinkage, which can be more clearly observed from the lateral view, as shown in Figure 4.2.10. The shrinkage after the heat treatment decreases with increasing sand content. Restraint by the bottom mortar layer, well-developed dense map cracking can be seen on all the samples.

Figure 4.2.10 Lateral view of NaMK-1.5 mortar sample after heat treatment.

Therefore, it can be concluded that additional sand can indeed improve the integrity of AAMs ceramic. However, optimization of mix proportion is needed to have a more homogenous sand content distribution along the thickness.

4.3 Flexural strength

Mixtures with relatively acceptable integrity were then tested for flexural strength by three-point bending. Based on the results from section 4.2, only part of the AAS mixtures has relatively acceptable integrity, as shown in Figure 4.2.6. The flexural strength results are shown in Table 4.3.1.

Table 4.3.1 Flexural strength of heat-treated AAS samples

Flexural strength (MPa)				
AAS Mixture		**Ms**		
		0	0.5	1
N/B	2%	-	-	3.03
	3%	-	1.35	2.00
	4%	1.05	1.12	N.A.

The flexural strength of AAS is too low to be used as ceramic tiles. Nevertheless, the magnitude conforms to the literature [37]. The flexural strength of a product depends on many factors. In this case, the low flexural strength is attributed to the existing cracking in the samples instead of the matrix itself. During grinding the samples for XRD, the materials became clearly stronger than before heat treatment. However, grains are clearly visible on the fracture surface morphology after the three-point bending test, as shown in Figure 4.3.1. This morphological characteristic indicated the pre-existing of well-developed internal cracking. Even the cracks were recovered by sintering to an extent. The bonding was still far weaker than the matrix.

Figure 4.3.1 Typical fracture surface morphology after three-point bending

The poor machinability while sawing the specimen also showed the existence of internal cracks. A typical sawed sample is shown in Figure 4.3.2. Although the surface showed good integrity, spalling of the fragments of the samples during sawing resulted in a very uneven cut surface, indicating that the samples are closer to a loose composite of many individual grains instead of a homogenous material.

Figure 4.3.2 Typical overview (upper) and cross-section (lower) of sawed sample

5 Conclusions and recommendations

5.1 Conclusions

In this study, the feasibility of fabricating building ceramic tiles with AAMs was preliminarily investigated from the perspective of crystallization, integrity, and mechanical properties.

From the perspective of crystallization, AAMs do have potential in fabricating building ceramic tiles. The contribution and significance of geopolymerization prior to heat treatment have also been confirmed by comparing different mixtures.

For the GP, samples with different Si/Al ratios were studied. Before heat treatment, Na-A zeolite and faujasite zeolite were found in the unheated green bodies of low Si/Al ratio mixtures. After thermal treatment at 800°C, crystallization of nepheline and low-carnegiete was found. Samples with Si/Al ratio $\leq$ 1.25 had a considerable extent of crystallization, while the samples with a higher Si/Al ratio remained primarily amorphous. The effect of curing time was also investigated on GP samples. Prolonging the curing time of NaMK-1.25 to 7 days resulted in the formation of Na-A zeolite, which was not detected in the 3-day curing sample. After heat treatment, the extent of crystallization of 1-day, 3-day, and 7-day samples is found to be positively correlated to the curing time (i.e., extent of reaction). Besides, the effect of curing temperature was also studied by the GP samples. It was found that the GP needed to be cured under a suitable temperature to have the highest extent of crystallization after heat treatment. In addition, it was also investigated that using RHA as an alternative silica source to replace the commercial sodium silicate solution in GP completely. The result is promising and comparable.

For the AAS, samples with different alkali dosages and modulus were studied. Crystallization of akermanite, merwhinite, and possible gehlenite was found after heat treatment. Due to the low extent of the reaction, the heated sample with the lowest alkali dosage showed a hump that belongs to unreacted slag, indicating the significance of geopolymerization reaction on crystallization. In contrast, the difference in XRD pattern between samples with high enough alkali dosage was less significant. On the other hand, by comparing the XRD patterns of NaS-(0-2)-4% samples, it can be observed that merwinite is the favored crystalline phase in a low Si-environment while akermanite is the favored crystalline phase in a higher Si environment.

From the perspective of integrity, cracking is a key issue for fabricating ceramic building tiles with as-cast AAMs. For all the samples, during the drying and heat treatment, cracks are generated by the capillary action and vapor pressure. Most of the samples did not show satisfactory integrity after heat treatment. Some of the samples showed acceptable integrity with the help of sintering but showed poor mechanical properties due to the internal cracks and poor bonding between recovered cracks. In order to reduce the cracking tendency, prolonging the curing and addition of sand were tried. For the samples that can remain relatively intact after the drying procedure, prolonging the curing can improve the integrity. In contrast, for the sample that has already cracked during the drying procedure, prolonging curing will only intensify the cracking issue due to the development of drying cracks. The addition of sand can significantly improve the integrity of products, but considerable segregation will be involved, and therefore careful optimization of mix proportion is needed.

5.2 Recommendations

It has been confirmed that alkali-activated technology does have merit in fabrication of ceramic tiles, and indeed capable to synthesis ceramic. However, crystallization is not the only aspect of ceramic tile. From the perspective of ceramic building tile, desirable properties are more important than crystallization. Regarding the ceramic tiles' resultant properties, the molding method (e.g., as-cast vs. powder metallurgy), and fabrication method has a significant influence. And based on the results of this preliminary study, it seems that the as-cast method will meet huge difficulties when it comes to real application. And therefore, it is suggested that the following study might base on the powder metallurgy method.

Using RHA as an alternative silica source is confirmed to be feasible in the study. Therefore, it is suggested to further study using the waste or by-products to substitute the commercial silicate solution and further reduce the environmental impact.

6 Reference

1. *World production and consumption of ceramic tiles*. 2021, ACIMAC Research Department.
2. Abdalqader, A.F., F. Jin, and A. Al-Tabbaa, *Development of greener alkali-activated cement: utilisation of sodium carbonate for activating slag and fly ash mixtures.* Journal of Cleaner Production, 2016. **113**: p. 66-75.
3. Ye, L., et al., *Life cycle environmental and economic assessment of ceramic tile production: A case study in China.* Journal of Cleaner Production, 2018. **189**: p. 432-441.
4. Kingery, W.D., H.K. Bowen, and D.R. Uhlmann, *Introduction to ceramics*. Vol. 17. 1976: John wiley & sons.
5. Tikul, N. and P. Srichandr, *Assessing the environmental impact of ceramic tile production in Thailand.* Journal of the Ceramic Society of Japan, 2010. **118**(1382): p. 887-894.
6. Boschi, G., et al., *Sustainability in Italian Ceramic Tile Production: Evaluation of the Environmental Impact.* Applied Sciences, 2020. **10**(24): p. 9063.
7. Shi, C., D. Roy, and P. Krivenko, *Alkali-Activated Cements and Concretes*. 2006: Taylor & Francis.
8. Davidovits, J., *Geopolymers: inorganic polymeric new materials.* Journal of Thermal Analysis and calorimetry, 1991. **37**(8): p. 1633-1656.
9. !!! INVALID CITATION !!! [9, 10].
10. He, P., et al., *Thermal evolution and crystallization kinetics of potassium-based geopolymer.* Ceramics International, 2011. **37**(1): p. 59-63.
11. Bell, J.L., P.E. Driemeyer, and W.M. Kriven, *Formation of Ceramics from Metakaolin-Based Geopolymers. Part II: K-Based Geopolymer.* Journal of the American Ceramic Society, 2009. **92**(3): p. 607-615.
12. He, P., D. Jia, and S. Wang, *Microstructure and integrity of leucite ceramic derived from potassium-based geopolymer precursor.* Journal of the European Ceramic Society, 2013. **33**(4): p. 689-698.
13. Bell, J.L., P.E. Driemeyer, and W.M. Kriven, *Formation of Ceramics from Metakaolin-Based Geopolymers: Part I—Cs-Based Geopolymer.* Journal of the American Ceramic Society, 2009. **92**(1): p. 1-8.
14. Martínez-Martínez, S., et al., *Influence of firing temperature on the ceramic properties of illite-chlorite-calcitic clays.* Ceramics International, 2022.
15. Shariff, K.A., et al. *Effect of Different Firing Temperature on Thermal Conductivity of Ceramic Tiles*. in *Materials Science Forum*. 2020. Trans Tech Publ.
16. Martín-Márquez, J., J.M. Rincón, and M. Romero, *Effect of firing temperature on sintering of porcelain stoneware tiles.* Ceramics International, 2008. **34**(8): p. 1867-1873.
17. CEN, *EN 14411:2016 Ceramic tiles - Definition, classification, characteristics, assessment and verification of constancy of performance and marking*. 2016.
18. ISO, *ISO 13006:2018(en)*

Ceramic tiles — Definitions, classification, characteristics and marking. 2018.

19. Xie, N., J.L. Bell, and W.M. Kriven, *Fabrication of structural leucite glass–ceramics from potassium-based geopolymer precursors.* Journal of the American Ceramic Society, 2010. **93**(9): p. 2644-2649.
20. !!! INVALID CITATION !!! [10, 11, 13, 20-23].
21. Duxson, P., G.C. Lukey, and J.S.J. van Deventer, *Thermal evolution of metakaolin geopolymers: Part 1 – Physical evolution.* Journal of Non-Crystalline Solids, 2006. **352**(52): p. 5541-5555.
22. Duxson, P., G.C. Lukey, and J.S.J. van Deventer, *Physical evolution of Na-geopolymer derived from metakaolin up to 1000 °C.* Journal of Materials Science, 2007. **42**(9): p. 3044-3054.
23. Guerrieri, M., J. Sanjayan, and F. Collins, *Residual compressive behavior of alkali-activated concrete exposed to elevated temperatures.* Fire and Materials: An International Journal, 2009. **33**(1): p. 51-62.
24. Mačiulaitis, R., A. Jefimovas, and P. Zdanevičius, *Research of natural wood combustion and charring processes.* Journal of Civil Engineering and Management, 2012. **18**(5): p. 631-641.
25. He, P., et al., *Effect of cesium substitution on the thermal evolution and ceramics formation of potassium-based geopolymer.* Ceramics International, 2010. **36**(8): p. 2395-2400.
26. Burciaga-Díaz, O. and J.I. Escalante-García, *Comparative performance of alkali activated slag/metakaolin cement pastes exposed to high temperatures.* Cement and Concrete Composites, 2017. **84**: p. 157-166.
27. Rashad, A.M., S.R. Zeedan, and A.A. Hassan, *Influence of the activator concentration of sodium silicate on the thermal properties of alkali-activated slag pastes.* Construction and Building Materials, 2016. **102**: p. 811-820.
28. Kapeluszna, E., et al., *Incorporation of Al in C-A-S-H gels with various Ca/Si and Al/Si ratio: Microstructural and structural characteristics with DTA/TG, XRD, FTIR and TEM analysis.* Construction and Building Materials, 2017. **155**: p. 643-653.
29. Rahier, H., et al., *Low-temperature synthesized aluminosilicate glasses.* Journal of materials science, 1996. **31**(1): p. 71-79.
30. Zarzycki, J., M. Prassas, and J. Phalippou, *Synthesis of glasses from gels: the problem of monolithic gels.* Journal of materials science, 1982. **17**(11): p. 3371-3379.
31. Duxson, P., et al., *Understanding the relationship between geopolymer composition, microstructure and mechanical properties.* Colloids and Surfaces A: Physicochemical and Engineering Aspects, 2005. **269**(1-3): p. 47-58.
32. Leko, V.K. and O.V. Mazurin, *Analysis of Regularities in Composition Dependence of the Viscosity for Glass-Forming Oxide Melts: II. Viscosity of Ternary Alkali Aluminosilicate Melts.* Glass Physics and Chemistry, 2003. **29**(1): p. 16-27.
33. Duxson, P., G.C. Lukey, and J.S.J. van Deventer, *Evolution of Gel Structure during Thermal Processing of Na-Geopolymer Gels.* Langmuir, 2006. **22**(21): p. 8750-8757.
34. Duxson, P., G.C. Lukey, and J.S.J. van Deventer, *The thermal evolution of metakaolin geopolymers: Part 2 – Phase stability and structural development.* Journal of Non-Crystalline Solids, 2007. **353**(22): p. 2186-2200.

35. Rahier, H., et al., *Low-temperature synthesized aluminosilicate glasses: Part III Influence of the composition of the silicate solution on production, structure and properties.* Journal of Materials Science, 1997. **32**(9): p. 2237-2247.

36. Puertas, F., et al., *Alkali-activated slag mortars reinforced with ar glassfibre. Performance and properties.* Materiales de Construcción, 2006. **56**(283): p. 79-90.

37. Rovnaník, P., P. Bayer, and P. Rovnaníková, *Characterization of alkali activated slag paste after exposure to high temperatures.* Construction and Building Materials, 2013. **47**: p. 1479-1487.

38. Bernal, S.A., et al., *Performance at high temperature of alkali-activated slag pastes produced with silica fume and rice husk ash based activators.* Materiales de Construcción, 2015. **65**(318): p. e049-e049.

39. Garcia-Lodeiro, I., et al., *Compatibility studies between N-A-S-H and C-A-S-H gels. Study in the ternary diagram Na2O–CaO–Al2O3–SiO2–H2O.* Cement and Concrete Research, 2011. **41**(9): p. 923-931.

40. Ahmad, R., et al., *Fabrication of lightweight ceramic materials using geopolymer technology*, in *Sustainable Waste Utilization in Bricks, Concrete, and Cementitious Materials*. 2021, Springer. p. 167-189.

41. Beleña, I. and W. Zhu, *Nanoindentation study of Na-geopolymers exposed to high temperatures*, in *Nanotechnology in Construction 3*. 2009, Springer. p. 169-174.

42. Kuenzel, C., et al., *Ambient Temperature Drying Shrinkage and Cracking in Metakaolin-Based Geopolymers.* Journal of the American Ceramic Society, 2012. **95**(10): p. 3270-3277.

43. Ahmad, R., et al., *Role of Sintering Temperature in Production of Nepheline Ceramics-Based Geopolymer with Addition of Ultra-High Molecular Weight Polyethylene.* Materials, 2021. **14**(5): p. 1077.

44. Ye, G., H. Huang, and N.V. Tuan, *Rice husk ash.* Properties of Fresh and Hardened Concrete Containing Supplementary Cementitious Materials, 2018: p. 283-302.

45. Huang, H., et al. *Use of rice husk ash for mitigating the autogenous shrinkage of cement pastes at low water cement ratio*. in *Proceedings of the HiPerMat 2016 4th international symposium on ultra-high performance concrete and high performance construction materials, Kassel, Germany*. 2016.

46. Chao-Lung, H., B. Le Anh-Tuan, and C. Chun-Tsun, *Effect of rice husk ash on the strength and durability characteristics of concrete.* Construction and building materials, 2011. **25**(9): p. 3768-3772.

47. Siddique, R., *Waste materials and by-products in concrete*. 2007: Springer Science & Business Media.

48. Van Tuan, N., et al., *Hydration and microstructure of ultra high performance concrete incorporating rice husk ash.* Cement and Concrete Research, 2011. **41**(11): p. 1104-1111.

49. Alonso, S. and A. Palomo, *Alkaline activation of metakaolin and calcium hydroxide mixtures: influence of temperature, activator concentration and solids ratio.* Materials Letters, 2001. **47**(1): p. 55-62.

50. Alonso, S. and A. Palomo, *Alkaline activation of metakaolin and calcium hydroxide mixtures: influence of temperature, activator concentration and solids ratio.* Materials Letters, 2001. **47**(1-2): p. 55-62.

51. Ismail, I., et al., *Drying-induced changes in the structure of alkali-activated pastes.* Journal of Materials Science, 2013. **48**(9): p. 3566-3577.

52. Cioffi, R., L. Maffucci, and L. Santoro, *Optimization of geopolymer synthesis by calcination and polycondensation of a kaolinitic residue.* Resources, conservation and recycling, 2003. **40**(1): p. 27-38.

53. Duxson, P., et al., *29Si NMR study of structural ordering in aluminosilicate geopolymer gels.* Langmuir, 2005. **21**(7): p. 3028-3036.

54. Rowles, M. and B. O'connor, *Chemical optimisation of the compressive strength of aluminosilicate geopolymers synthesised by sodium silicate activation of metakaolinite.* journal of Materials Chemistry, 2003. **13**(5): p. 1161-1165.

55. Wang, Y., et al., *Study of acidic degradation of alkali-activated materials using synthetic C-(N)-ASH and NASH gels.* Composites Part B: Engineering, 2022. **230**: p. 109510.

56. Rhodes, C.J., *Properties and applications of Zeolites.* Science Progress, 2010. **93**(3): p. 223-284.

57. Bowen, J.F.F.N.F., *The System NA2O -- al2o3-- SIO2*. 1956: Kline Geology Laboratory, Yale University.

58. Barbosa, V.F. and K.J. MacKenzie, *Thermal behavior of inorganic geopolymers and composites derived from sodium polysialate.* Materials research bulletin, 2003. **38**(2): p. 319-331.

59. Walkley, B., et al., *Examination of alkali-activated material nanostructure during thermal treatment.* Journal of materials science, 2018. **53**(13): p. 9486-9503.

60. Nayak, M. and T. Kutty, *Luminescence of Fe3+ doped NaAlSiO4 prepared by gel to crystallite conversion.* Materials chemistry and physics, 1998. **57**(2): p. 138-146.

61. Ohgushi, T., K. Ishimaru, and S. Komarneni, *Nepheline and carnegieite ceramics from A-Type zeolites by microwave heating.* Journal of the American Ceramic Society, 2001. **84**(2): p. 321-27.

62. Dimitrijevic, R., et al., *Structural characterization of pure Na-nephelines synthesized by zeolite conversion route.* Journal of Physics and Chemistry of Solids, 2004. **65**(10): p. 1623-1633.

63. Radulović, A., et al., *Thermal transformation of Na-LTA zeolite into low-carnegieite: The influence of residual sodium and aluminium species.* Thermochimica acta, 2010. **511**(1-2): p. 37-42.

64. Kuenzel, C., et al., *Production of nepheline/quartz ceramics from geopolymer mortars.* Journal of the European Ceramic Society, 2013. **33**(2): p. 251-258.

65. Schneider, H., O. Flörke, and R. Stoeck, *The NaAlSiO4 nepheline-carnegieite solid-state transformation.* Zeitschrift für Kristallographie-Crystalline Materials, 1994. **209**(2): p. 113-117.

66. Kosanovic, C., B. Subotic, and I. Smit, *Thermally induced phase transformations in cation-exchanged zeolites 4A, 13X and synthetic mordenite and their amorphous derivatives obtained by mechanochemical treatment.* Thermochimica Acta, 1998. **317**(1): p. 25-37.

67. Jeleń, P., *The Effect of Heat Treatment on the Structure of Zeolite A.* Materials, 2021. **14**(16): p. 4642.

68. Lutz, W., et al., *The influence of water steam on the direct phase transformation of zeolite NaA to nepheline by thermal treatment.* Crystal Research and Technology, 1985. **20**(9): p. 1217-1223.

69. Zhang, M., et al., *Modeling the polymerization process for geopolymer synthesis through reactive molecular dynamics simulations.* The Journal of Physical Chemistry C, 2018. **122**(12): p. 6760-6773.

70. Chen, C.-T., et al., *Reaction kinetics regulated formation of short-range order in an amorphous matrix during zeolite crystallization.* Journal of the American Chemical Society, 2021. **143**(29): p. 10986-10997.

71. Weng, L. and K. Sagoe-Crentsil, *Dissolution processes, hydrolysis and condensation reactions during geopolymer synthesis: Part I—Low Si/Al ratio systems.* Journal of materials science, 2007. **42**(9): p. 2997-3006.

72. Yao, X., et al., *Geopolymerization process of alkali–metakaolinite characterized by isothermal calorimetry.* Thermochimica Acta, 2009. **493**(1-2): p. 49-54.

73. Aredes, F.G.M., et al., *Effect of cure temperature on the formation of metakaolinite-based geopolymer.* Ceramics International, 2015. **41**(6): p. 7302-7311.

74. Puertas, F., et al., *Morteros de escoria activada alcalinamente reforzados con fibra de vidrio AR. Comportamiento y propiedades*. 2006, Consejo Superior de Investigaciones Científicas (España).

75. Walkley, B., et al., *Phase evolution of C-(N)-ASH/NASH gel blends investigated via alkali-activation of synthetic calcium aluminosilicate precursors.* Cement and Concrete Research, 2016. **89**: p. 120-135.

76. Bernal, S.A., et al., *Gel nanostructure in alkali-activated binders based on slag and fly ash, and effects of accelerated carbonation.* Cement and Concrete Research, 2013. **53**: p. 127-144.

77. Wang, S.-D. and K.L. Scrivener, *Hydration products of alkali activated slag cement.* Cement and Concrete Research, 1995. **25**(3): p. 561-571.

78. Shi, Z., et al., *Effect of alkali dosage and silicate modulus on carbonation of alkali-activated slag mortars.* Cement and Concrete Research, 2018. **113**: p. 55-64.

79. Ervin Jr, G. and E.F. Osborn, *X-ray data on synthetic melilites.* American Mineralogist: Journal of Earth and Planetary Materials, 1949. **34**(9-10): p. 717-722.

80. Swainson, I.P., et al., *Neutron powder diffraction study of the åkermanite-gehlenite solid solution series.* Physics and Chemistry of Minerals, 1992. **19**(3): p. 185-195.

81. Tavangarian, F., et al., *Facile synthesis and structural insight of nanostructure akermanite powder.* Ceramics International, 2019. **45**(6): p. 7871-7877.

82. Kuenzel, C., et al., *Ambient temperature drying shrinkage and cracking in metakaolin-based geopolymers.* Journal of the American Ceramic Society, 2012. **95**(10): p. 3270-3277.

83. Perera, D., et al., *Influence of curing schedule on the integrity of geopolymers.* Journal of materials science, 2007. **42**(9): p. 3099-3106.

84. Park, S. and M. Pour-Ghaz, *What is the role of water in the geopolymerization of metakaolin?* Construction and Building Materials, 2018. **182**: p. 360-370.

85. Scherer, G.W., *Theory of drying.* Journal of the American Ceramic Society, 1990. **73**(1): p. 3-14.

86. Li, Z., et al., *Mechanisms of autogenous shrinkage of alkali-activated slag and fly ash pastes.* Cement and Concrete Research, 2020. **135**: p. 106107.

87. Phan, L.T., *Pore pressure and explosive spalling in concrete.* Materials and structures, 2008. **41**(10): p. 1623-1632.

88. Kalifa, P., F.-D. Menneteau, and D. Quenard, *Spalling and pore pressure in HPC at high temperatures.* Cement and concrete research, 2000. **30**(12): p. 1915-1927.

89. Mindeguia, J.-C., et al., *Temperature, pore pressure and mass variation of concrete subjected to high temperature—Experimental and numerical discussion on spalling risk.* Cement and concrete research, 2010. **40**(3): p. 477-487.

90. Samouh, H., et al., *Consequences of longer sealed curing on drying shrinkage, cracking and carbonation of concrete.* Cement and Concrete Research, 2017. **95**: p. 117-131.

91. de Sa, C., et al., *Analysis of microcracking induced by differential drying shrinkage.* Cement and Concrete Composites, 2008. **30**(10): p. 947-956.

92. Collins, F. and J. Sanjayan, *Microcracking and strength development of alkali activated slag concrete.* Cement and Concrete Composites, 2001. **23**(4-5): p. 345-352.

93. Lee, N., J.G. Jang, and H.-K. Lee, *Shrinkage characteristics of alkali-activated fly ash/slag paste and mortar at early ages.* Cement and Concrete Composites, 2014. **53**: p. 239-248.

94. Ye, H. and A. Radlińska, *Shrinkage mitigation strategies in alkali-activated slag.* Cement and Concrete Research, 2017. **101**: p. 131-143.